

# Flow-matching Operators for Residual-Augmented Probabilistic Learning of Partial Differential Equations

Sahil Bhola, Karthik Duraisamy

*Department of Aerospace Engineering & Michigan Institute for Computational Discovery and Engineering,  
University of Michigan, Ann Arbor, U.S.A.*

---

## Abstract

Learning probabilistic surrogates for PDEs remains challenging in data-scarce regimes: neural operators require large amounts of high-fidelity data, while generative approaches typically sacrifice resolution invariance. We formulate flow matching in an infinite-dimensional function space to learn a probabilistic transport that maps low-fidelity approximations to the manifold of high-fidelity PDE solutions via learned residual corrections. We develop a conditional neural operator architecture based on feature-wise linear modulation for flow-matching vector fields directly in function space, enabling inference at arbitrary spatial resolutions without retraining. To improve stability and representational control of the induced neural ODE, we parameterize the flow vector field as a sum of a linear operator and a nonlinear operator, combining lightweight linear components with a conditioned Fourier neural operator for expressive, input-dependent dynamics. We then formulate a residual-augmented learning strategy where the flow model learns probabilistic corrections from inexpensive low-fidelity surrogates to high-fidelity solutions, rather than learning the full solution mapping from scratch. Finally, we derive tractable training objectives that extend conditional flow matching to the operator setting with input-function-dependent couplings. To demonstrate the effectiveness of our approach, we present numerical experiments on a range of PDEs, including the 1D advection and Burgers' equation, and a 2D Darcy flow problem for flow through a porous medium. We show that the proposed method can accurately learn solution operators across different resolutions and fidelities and produces uncertainty estimates that appropriately reflect model confidence, even when trained on limited high-fidelity data.

---

## 1. Introduction

Solving partial differential equations (PDEs) is fundamental for understanding and predicting complex physical systems, yet they remain prohibitively expensive for applications such as design optimization, uncertainty quantification, real-time inference, and predictive control. Traditional numerical methods, such as finite element and finite difference methods, require explicit domain discretization, which introduces an inherent trade-off between computational cost and solution accuracy [1, 2]. Recent advances in data-driven [3, 4, 5] and physics-informed machine learning [6, 7] have emerged as promising alternatives by leveraging data and physical priors to accelerate PDE solutions. Despite computational advantages over traditional approaches, the predictive capabilities of such methods are limited by the large amount of high-fidelity training data and often require retraining across different inputs of a PDE (for example, different initial conditions or coefficients). Moreover, most existing learning-based approaches are designed for fixed resolution inference and lack principled quantification of uncertainty in the predictions due to *inherent stochasticity* and *extrinsic uncertainty* in the physical system. This limits their practicality in high-resolution or data-scarce regimes, where quantifying uncertainty in predictions is paramount. While low-fidelity models (for example, simplified physics or coarser discretization) are widely available at reduced computational cost, present learning-based methods lack a mechanism to effectively leverage multi-fidelity sources of data while remaining resolution invariant and uncertainty-aware. As a result, there remains a need for a unified, data-efficient framework that can quantify uncertainty in the predictions, generate reliable predictions across arbitrary resolutions, and can flexibly incorporate multi-fidelity information.

Broadly, existing data-driven or physics-informed learning approaches fall into four classes: (a) finite-dimensional operators, (b) neural FEM, (c) neural operators, and (d) generative models. Finite-dimensional operator learning based methods seek to learn a deterministic mapping between finite-

dimensional Euclidean spaces, typically from the discrete input to the corresponding PDE solution. This approach includes convolution neural networks [8, 9, 10, 11, 12, 13] and latent space models [14, 15]. However, such methods are inherently resolution-dependent, which limits their flexibility for practical applications. Neural FEM methods address this by directly parameterizing the PDE solution function [16, 17, 18, 6]. While these methods are resolution-invariant, they must be retrained for each input of the PDE (for example, a change in initial condition or coefficients), which results in similar challenges observed in traditional numerical solvers [19]. Moreover, as with finite-dimensional operators, these methods yield deterministic PDE solution approximations. To address the need for resolution-invariance, neural operator-based methods parameterize the operator mapping between infinite-dimensional input and solution Hilbert function space using neural networks. Methods include DeepONet [20], FNO [21], and GNO [22]. By learning the operator between function spaces, these methods can infer PDE solutions at arbitrary resolution for any input to the PDE without retraining. However, similar to the finite-dimensional operators and neural FEM, these methods yield a deterministic operator mapping and therefore require post-hoc Monte Carlo sampling [9, 23], dropout [24, 25], noise injection [26, 27], or Laplace approximation [28, 29] to quantify uncertainty in the predictions. This dramatically becomes computationally expensive or inaccurate for complex high-dimensional PDEs. To quantify uncertainty in the predictions, generative models such as GANs [30, 31], diffusion models [32, 33], and flow-matching [34, 35] have shown significant promise by modeling the PDE solution as a random variable and seeking to learn the probability distribution using limited realizations of the input-solution pair. Specifically, by learning a probability distribution over the PDE solution conditioned on the inputs, such approaches overcome the need for model retraining as inputs change. They can also naturally account for the inherent stochasticity and extrinsic uncertainty (e.g., uncertain initial or boundary conditions) in the physical system. Such methods have shown significant promise in generating high-fidelity PDE datasets for Navier-Stokes [36, 37, 38, 39], porous media flow [40, 41], and weather forecasting [42, 43] where quantification of uncertainty in the predictions is essential for decision-making.

Despite the widespread success of generative models for PDEs, most existing approaches implicitly assume that the data distribution is supported on a finite-dimensional space for which probability distributions are well defined. As a result, similar to finite-dimensional operators, these methods become resolution-dependent and require model retraining to adapt to different discretizations. More recently, several efforts have sought to bridge generative models and neural operators to enable *probabilistic modeling of functional data*, including stochastic process observations and PDE solutions that naturally reside in function spaces. For example, GANO [44] models the generator and discriminator as FNO to enable sampling from Gaussian random fields. Similarly, extension of diffusion models to learn push-forwards of probability measures in infinite-dimensional Hilbert spaces has been studied and successfully applied to a wide range of PDEs and functional datasets [45, 46, 47, 48]. However, methods based on GANs and diffusion models often face challenges, including training instability, computationally expensive inference, and sensitivity to input conditioning. To address this, flow-matching-based operators have been proposed that learn a deterministic continuous-time transport map between infinite-dimensional function spaces [49, 50, 51]. Unlike GANs or diffusion models, flow-matching-based operators define a deterministic vector-field operator that induces a push-forward probability measure to approximate the probability measure induced by the functional data. As a result, generating function samples only require solving an ordinary differential equation (ODE) using the learned vector field, leading to efficient and stable inference. *While these methods have shown substantial potential in modeling functional data, they often require large amounts of high-fidelity training data and ignore the availability of computationally-inexpensive low-fidelity models that can serve as useful inductive bias.*

In this work, we propose a novel framework that integrates flow-matching-based neural operators with multi-fidelity learning to construct a data-efficient, uncertainty-aware, and resolution-invariant surrogate for PDE solutions. The key idea is to leverage low-fidelity function approximations with probabilistic residual learning to fuse functional datasets of varying fidelity, thereby enabling the proposed methodology to learn complex PDEs in a computationally efficient manner. In summary, our key contributions are as follows:

1. **Conditional Neural Operator for Flow-matching Vector Field:** We introduce a conditional neural operator that allows the model to generate solutions at arbitrary spatial resolution using flow-matching. This eliminates the need to train separate operators for each grid and input

to the PDE, enabling flexible inference across discretizations.

2. **Residual-Augmented Flow Models for Scientific Prediction:** We propose a novel formulation in which the flow model learns the correction (residual) between a low-fidelity surrogate and the high-fidelity solution. This significantly improves data efficiency, reduces predictive variance, and enables principled uncertainty estimates through the flow map.
3. **A Unified Framework for Uncertainty-Aware Multi-Resolution Surrogates:** Together, these components yield a probabilistic generative surrogate that produces coherent samples across fidelities and resolutions, with calibrated uncertainty and strong performance in data-limited settings.
4. **Empirical Validation on PDEs:** We demonstrate the effectiveness of our approach on several benchmark PDE problems, including the advection equation, Burgers’ equation, and Darcy flow, showing significant improvements in accuracy and uncertainty quantification by leveraging multi-fidelity information.

We organize the manuscript as follows. We provide the high level problem statement and necessary background on neural operators and flow-matching in §2. In §3, we first present a finite-dimensional perspective of generating probabilistic PDE solutions using flow-matching. Next, we introduce the operator view of flow-matching for functional PDE solutions and present our proposed flow-matching operator for residual-augmented learning. We demonstrate the effectiveness of our approach on several benchmark PDE problems in §4, followed by concluding remarks in §5.

## 2. Background

Our goal is to solve the *forward problem*, that is, to obtain the solution of any PDE given an input function (such as boundary conditions, initial condition, or input forcing). Mathematically, a PDE with an unknown solution function  $w \in \mathcal{W} \triangleq \{w : \Omega_w \subset \mathbb{R}^{\kappa_w} \rightarrow \mathbb{R}^{m_w}\}$  and input function  $a \in \mathcal{A} \triangleq \{a : \Omega_a \subset \mathbb{R}^{\kappa_a} \rightarrow \mathbb{R}^{m_a}\}$  can be expressed as

$$\mathcal{L}[w, a] = 0,$$

where  $\mathcal{L} : (\mathcal{W} \times \mathcal{A}) \rightarrow \mathcal{R}$  is the residual operator that maps the solution-input pair to the residual function space  $\mathcal{R} \triangleq \{r : \Omega_w \subset \mathbb{R}^{\kappa_w} \rightarrow \mathbb{R}^{m_r}\}$ . When the problem is well-posed there exists a *deterministic solution operator*  $\mathcal{G} : \mathcal{A} \rightarrow \mathcal{W}$  such that  $\mathcal{L}[\mathcal{G}[a], a] = 0$  for all  $a \in \mathcal{A}$ . That is, the solution  $w$  is a push forward of the input function  $a$  under the operator  $\mathcal{G}$ . To solve the forward problem, for both time-independent and time-dependent PDEs, we seek to obtain the solution  $w$  or trajectory  $\{w(t) : t \geq 0\}$  for a given input  $a$ . Relevant background work is summarized in the subsections below.

### 2.1. Neural Operators for solving Partial Differential Equations

Neural operators solve the forward problem by learning the mapping between infinite-dimensional function spaces, offering a mesh-independent and data-efficient alternative to traditional PDE solvers and neural-network-based approaches. Mathematically, for a real and separable Hilbert input and solution function space  $\mathcal{A}$  and  $\mathcal{W}$ , respectively, neural operators seek a parametric approximation to the solution operator  $\mathcal{G}$ . Given an input function  $a \in \mathcal{A}$ , the parametric approximation  $\mathcal{G}^\theta[a]$  with parameters  $\theta \in \mathbb{R}^{n_\theta}$  seeks to approximate the PDE solution function  $w = \mathcal{G}[a] \in \mathcal{W}$ . Unlike classical neural networks that learn mappings between finite-dimensional approximations of the input and solution functions, neural operators generalize parametric function approximation to learn mappings between infinite-dimensional function spaces. As a result, the solution function  $w$  can be inferred for any  $x_w \in \Omega_w$  for all  $a \in \mathcal{A}$  without the need for model retraining. Given finite realizations  $\{a^{(i)} \in \mathcal{A}\}_{i=1}^\ell$  and  $\{w^{(i)} \in \mathcal{W}\}_{i=1}^\ell$  drawn from the input and solution function spaces, neural operators approximate  $\mathcal{G}$  by minimizing the loss

$$J_{\text{NO}}(\theta) = \frac{1}{\ell} \sum_{i=1}^{\ell} \|\mathcal{G}^\theta[a^{(i)}] - \mathcal{G}[a^{(i)}]\|_{\mathcal{W}}^2,$$

which parallels the classical finite-dimensional learning framework.

## 2.2. Flow-Matching for Probabilistic Generative Modeling

Consider a realization  $\mathbf{y} \in \mathcal{Y}$  of a random variable  $\mathbf{Y} : \Omega \rightarrow \mathbb{R}^{d_y}$  with distribution  $p(\mathbf{y})$ , where  $\mathcal{Y} \subseteq \mathbb{R}^{d_y}$  denotes the set of all possible realizations of the random variable. Here, we use the same lowercase, uppercase, and symbol fonts to denote the realization, random variable, and set of realizations, respectively. In probabilistic generative modeling, the objective is to approximate the *data distribution*  $p(\mathbf{y})$  given a finite set of realizations  $\{\mathbf{y}^i \sim p(\mathbf{y})\}_{i=1}^{\xi}$ . Continuous normalizing flows [52, 53] constitute a class of generative models that achieve this by continuously transforming a *prior distribution*  $\pi(\mathbf{y})$  via a parameterized, time-dependent diffeomorphic map, called *flow*. Formally, the flow is defined as  $\phi^\zeta : [0, 1] \times \mathbb{R}^{d_y} \rightarrow \mathbb{R}^{d_y}$  that acts as  $(\tau, \mathbf{y}) \mapsto \phi_\tau^\zeta(\mathbf{y}, \tau)$  with  $\phi_\tau^\zeta : \mathbb{R}^{d_y} \rightarrow \mathbb{R}^{d_y}$  and time  $\tau \in [0, 1]$ . Here,  $\zeta \in \mathbb{R}^{n_\zeta}$  are the flow parameters that dictate the continuous transformation. Given a vector field  $u^\zeta : [0, 1] \times \mathbb{R}^{d_y} \rightarrow \mathbb{R}^{d_y}$  that acts as  $(\tau, \mathbf{y}) \mapsto u_\tau^\zeta(\mathbf{y})$  with  $u_\tau^\zeta : \mathbb{R}^{d_y} \rightarrow \mathbb{R}^{d_y}$ , the flow transformation is characterized by the ordinary differential equation (ODE)

$$\begin{aligned} \frac{d}{d\tau} \phi_\tau^\zeta(\mathbf{y}) &= u_\tau^\zeta(\phi_\tau^\zeta(\mathbf{y})), \quad \tau \in [0, 1], \\ \phi_0^\zeta(\mathbf{y}) &= \mathbf{y} \sim \pi(\mathbf{y}). \end{aligned}$$

Such a continuous transformation induces the push-forward  $q_\tau(\mathbf{y}; \zeta) \triangleq [\phi_\tau^\zeta]_{\#} \pi(\mathbf{y})$ , where  $q_\tau(\mathbf{y}; \zeta) : [0, 1] \times \mathbb{R}^{d_y} \rightarrow \mathbb{R}_{>0}$  is the time-varying *marginal probability path*. Any vector field  $u_\tau^\zeta$  that induces such a probability path must satisfy the continuity equation (see Appendix A). To approximate the data distribution, we seek a vector field  $u_\tau^\zeta$  that induces a probability path  $q_\tau(\mathbf{y}; \zeta)$  such that  $q_1(\mathbf{y}; \zeta) \approx p(\mathbf{y})$ .

In the case where we can tractably sample from the induced probability path  $q_\tau(\mathbf{y}; \zeta)$  and evaluate the vector field  $u_\tau^\zeta(\mathbf{y})$  for all  $\tau \in [0, 1]$ , we can learn a parameterized vector field  $v_\tau^\zeta : \mathbb{R}^{d_y} \rightarrow \mathbb{R}^{d_y}$ , with parameters  $\xi \in \mathbb{R}^{n_\xi}$ , by minimizing the *flow matching* (FM) objective

$$J_{\text{FM}}(\zeta, \xi) \triangleq \mathbb{E}_{\tau \sim \mathcal{U}[0,1], \mathbf{y} \sim q_\tau(\mathbf{y}; \zeta)} [\|u_\tau^\zeta(\mathbf{y}) - v_\tau^\zeta(\mathbf{y})\|_2^2], \quad (1)$$

as proposed in [34]. Upon reaching the optimal parameters  $\xi^*$  for which  $J_{\text{FM}}(\zeta, \xi^*) = 0$ , the learned vector field  $v_\tau^{\xi^*}$  induces the same probability path  $q_\tau(\mathbf{y}; \zeta)$  as  $u_\tau^\zeta$ . However, in practice the vector field  $u_\tau^\zeta(\mathbf{y})$  that induces the probability path  $q_\tau(\mathbf{y}; \zeta)$  with  $q_1(\mathbf{y}; \zeta) \approx p(\mathbf{y})$  is unknown. To address this, [35] introduced a latent random variable  $\mathbf{Z} : \Omega \rightarrow \mathbb{R}^{d_z}$  with distribution  $q(\mathbf{z})$  to define a vector field  $\tilde{u}^\zeta : [0, 1] \times \mathbb{R}^{d_y} \times \mathbb{R}^{d_z} \rightarrow \mathbb{R}^{d_y}$  that acts as  $(\tau, \mathbf{y}, \mathbf{z}) \mapsto \tilde{u}_{\tau, \mathbf{z}}^\zeta(\mathbf{y})$  with  $\tilde{u}_{\tau, \mathbf{z}}^\zeta : \mathbb{R}^{d_y} \rightarrow \mathbb{R}^{d_y}$ . Given the vector field  $\tilde{u}_{\tau, \mathbf{z}}^\zeta$  induces the conditional probability path  $q_\tau(\mathbf{y}|\mathbf{z}; \zeta)$  via the continuity equation for each  $\mathbf{z} \in \mathbb{R}^{d_z}$ , we can define the marginal probability path  $q_\tau(\mathbf{y}; \zeta)$  as

$$q_\tau(\mathbf{y}; \zeta) \triangleq \int q_\tau(\mathbf{y}|\mathbf{z}; \zeta) q(\mathbf{z}) d\mathbf{z},$$

via marginalization. As a result, we can define the vector field  $u_\tau^\zeta$  as

$$u_\tau^\zeta \triangleq \mathbb{E}_{q(\mathbf{z})} \left[ \frac{\tilde{u}_{\tau, \mathbf{z}}^\zeta q_\tau(\mathbf{y}|\mathbf{z}; \zeta)}{q_\tau(\mathbf{y}; \zeta)} \right], \quad (2)$$

that also induces the marginal probability path  $q_\tau(\mathbf{y}; \zeta)$ , as shown in [35]. However, defining  $u_\tau^\zeta$  using eq. (2) still results in an intractable  $J_{\text{FM}}$  as the denominator  $q_\tau(\mathbf{y}; \zeta)$  requires marginalization. To address this, [35] proposed an unbiased objective, called the *conditional flow matching* (CFM) objective, given as

$$J_{\text{CFM}}(\zeta, \xi) \triangleq \mathbb{E}_{\tau \sim \mathcal{U}[0,1], \mathbf{z} \sim q(\mathbf{z}), \mathbf{y} \sim q_\tau(\mathbf{y}|\mathbf{z}; \zeta)} [\|\tilde{u}_{\tau, \mathbf{z}}^\zeta(\mathbf{y}) - v_\tau^\zeta(\mathbf{y})\|_2^2], \quad (3)$$

where  $\nabla_\xi J_{\text{CFM}}(\zeta, \xi) = \nabla_\xi J_{\text{FM}}(\zeta, \xi)$ . Thus, if we can tractably sample from the distributions  $q_\tau(\mathbf{y}|\mathbf{z}; \zeta)$  and  $q(\mathbf{z})$ , we can learn a vector field  $v_\tau^\zeta$  that induces the marginal probability path  $q_\tau(\mathbf{y}; \zeta)$  by minimizing  $J_{\text{CFM}}$ . To tractably sample from the conditional probability path  $q_\tau(\mathbf{y}|\mathbf{z}; \zeta)$ , [35] modeled the latent distribution as a joint distribution  $q(\mathbf{z}) = \pi(\mathbf{y})p(\mathbf{y})$ . As a result, the conditional probability path can be modeled as a transport of a Gaussian distribution given as

$$\begin{aligned} q_\tau(\mathbf{y}|\mathbf{z}; \zeta) &= \mathcal{N}(\mathbf{y}; \mu_\tau(\mathbf{z}), \sigma_\tau(\mathbf{z}; \zeta)), \\ \mu_\tau(\mathbf{z}) &\triangleq \tau \mathbf{y}_1 + (1 - \tau) \mathbf{y}_0, \quad \mathbf{y}_0 \sim \pi(\mathbf{y}), \mathbf{y}_1 \sim p(\mathbf{y}), \\ \sigma_\tau(\mathbf{z}; \zeta) &\triangleq \sigma_{\min}, \end{aligned}$$

where  $\zeta = \sigma_{\min}$  is a hyper-parameter that controls the smoothness of the probability path  $q_\tau(\mathbf{y}; \zeta)$  composed using the conditional probability path  $q_\tau(\mathbf{y}|\mathbf{z}; \zeta)$ . By defining the conditional probability path as a transport of Gaussian distributions, we can evaluate the vector field  $\tilde{u}_{\tau, \mathbf{z}}^\zeta$  in closed form as

$$\tilde{u}_{\tau, \mathbf{z}}^\zeta(\mathbf{y}) = \frac{\partial \sigma_\tau(\mathbf{z}; \zeta)}{\partial \tau} \frac{(\mathbf{y} - \mu_\tau(\mathbf{z}))}{\sigma_\tau(\mathbf{z}; \zeta)} + \frac{\partial \mu_\tau(\mathbf{z})}{\partial \tau}, \quad (4)$$

as shown in [35].

### 3. Methodology

In this section, we establish the mathematical framework for generating PDE solutions via flow-matching. We begin with a classical finite-dimensional perspective that produces a discrete yet probabilistic PDE solution on a discrete solution domain. We then extend the classical view to an operator view that enables probabilistic inference of PDE solution functions for any  $x_w \in \Omega_w$  and  $a \in \mathcal{A}$ . Lastly, we present a flow-matching operator for residual-augmented learning of PDEs, called FLORAL, that leverages low-fidelity data to enhance the data-efficiency of learning probabilistic neural operators via flow-matching.

#### 3.1. Finite-dimensional view of generating PDE solutions with uncertainty quantification

To make the problem of obtaining the solution function  $w$  tractable, often the domains  $\Omega_w$  and  $\Omega_a$  are discretized using finite points or basis functions (for example, using finite-difference or finite-element methods). Consider the point evaluation operators  $\mathcal{E}_a^{n_a} : \mathcal{A} \rightarrow \mathbb{R}^{d_a}$  and  $\mathcal{E}_w^{n_w} : \mathcal{W} \rightarrow \mathbb{R}^{d_w}$  defined as  $\mathcal{E}_a^{n_a}[a] = (a(x_a^1), \dots, a(x_a^{n_a}))^T \triangleq \mathbf{a}$  and  $\mathcal{E}_w^{n_w}[w] = (w(x_w^1), \dots, w(x_w^{n_w}))^T \triangleq \mathbf{w}$ , respectively. Here,  $\{x_a^i\}_{i=1}^{n_a} \subset \Omega_a$  and  $\{x_w^i\}_{i=1}^{n_w} \subset \Omega_w$  denote the discretization points of the input and solution domains, respectively, and  $d_w \triangleq m_w n_w$  and  $d_a \triangleq m_a n_a$  denote the dimensions of the discrete solution and input. Then, we can approximate the continuous residual operator  $\mathcal{L}$  by a discrete residual operator  $\hat{\mathcal{L}}$

$$\hat{\mathcal{L}}(\mathbf{w}, \mathbf{a}) = \mathbf{0},$$

where  $\hat{\mathcal{L}} : \mathbb{R}^{d_w} \times \mathbb{R}^{d_a} \rightarrow \mathbb{R}^{d_r}$  acts as  $(\mathbf{w}, \mathbf{a}) \mapsto \hat{\mathcal{L}}(\mathbf{w}, \mathbf{a})$ , where  $\hat{\mathcal{L}}(\mathbf{w}, \mathbf{a}) \in \mathbb{R}^{d_r}$  and  $d_r = m_r n_w$ . In such a discrete setting, the solution operator  $\mathcal{G}$  is approximated using the discrete solution function  $\hat{\mathcal{G}} : \mathbb{R}^{d_a} \rightarrow \mathbb{R}^{d_w}$  such that  $\hat{\mathcal{L}}(\hat{\mathcal{G}}(\mathbf{a}), \mathbf{a}) = \mathbf{0}$ . The goal of the forward problem is to determine the discrete solution  $\mathbf{w} = \hat{\mathcal{G}}(\mathbf{a})$  for a given discrete input  $\mathbf{a}$ .

To solve the forward problem in a probabilistic framework, we can model the solution  $\mathbf{w} = \hat{\mathcal{G}}(\mathbf{a})$  as a random variable with distribution  $p(\mathbf{w}|\mathbf{a})$  where  $\mathbf{a} \sim p(\mathbf{a})$ . In practice, we often have finite realizations of the joint distribution  $(\mathbf{w}, \mathbf{a}) \sim p(\mathbf{w}|\mathbf{a})p(\mathbf{a})$  obtained from numerical solvers or experimental measurements. Given a prior distribution  $\pi(\mathbf{w})$  on the PDE solution, we can construct a parameterized, time-dependent diffeomorphic *conditional flow*  $\psi^\zeta : [0, 1] \times \mathbb{R}^{d_w} \times \mathbb{R}^{d_a} \rightarrow \mathbb{R}^{d_w}$  that acts as  $(\tau, \mathbf{w}, \mathbf{a}) \mapsto \psi_{\tau, \mathbf{a}}^\zeta(\mathbf{w})$ , where  $\psi_{\tau, \mathbf{a}}^\zeta : \mathbb{R}^{d_w} \rightarrow \mathbb{R}^{d_w}$ . Similarly, consider a time-varying vector field  $f^\zeta : [0, 1] \times \mathbb{R}^{d_w} \times \mathbb{R}^{d_a} \rightarrow \mathbb{R}^{d_w}$  that acts as  $(\tau, \mathbf{w}, \mathbf{a}) \mapsto f_{\tau, \mathbf{a}}^\zeta(\mathbf{w})$ , where  $f_{\tau, \mathbf{a}}^\zeta : \mathbb{R}^{d_w} \rightarrow \mathbb{R}^{d_w}$ , that characterizes the conditional ODE

$$\begin{aligned} \frac{d}{d\tau} \psi_{\tau, \mathbf{a}}^\zeta(\mathbf{w}) &= f_{\tau, \mathbf{a}}^\zeta(\psi_{\tau, \mathbf{a}}^\zeta(\mathbf{w})), \quad \tau \in [0, 1], \\ \psi_{0, \mathbf{a}}^\zeta(\mathbf{w}) &= \mathbf{w} \sim \pi(\mathbf{w}). \end{aligned}$$

Such a conditional flow results in the push-forward  $q_\tau(\mathbf{w}|\mathbf{a}; \zeta) \triangleq [\psi_{\tau, \mathbf{a}}^\zeta]_{\#} \pi(\mathbf{w})$ , where  $q_\tau(\mathbf{w}|\mathbf{a}; \zeta) : [0, 1] \times \mathbb{R}^{d_w} \rightarrow \mathbb{R}_{>0}$  is the induced marginal probability path. To approximate the conditional data distribution  $p(\mathbf{w}|\mathbf{a})$ , we seek a vector field  $f_{\tau, \mathbf{a}}^\zeta$  that induces a conditional probability path  $q_\tau(\mathbf{w}|\mathbf{a}; \zeta)$  such that  $q_1(\mathbf{w}|\mathbf{a}; \zeta) \approx p(\mathbf{w}|\mathbf{a})$  for all  $\mathbf{a} \sim p(\mathbf{a})$ .

Following the FM objective, we can learn a parametric vector field  $h_{\tau, \mathbf{a}}^\xi : \mathbb{R}^{d_w} \rightarrow \mathbb{R}^{d_w}$  informed by the input  $\mathbf{a}$ , with parameters  $\xi \in \mathbb{R}^{n_\xi}$  by minimizing the empirical loss

$$J_{\text{PDE-FM}}(\zeta, \xi) \triangleq \mathbb{E}_{\tau \sim \mathcal{U}[0, 1], \mathbf{a} \sim p(\mathbf{a}), \mathbf{w} \sim q_\tau(\mathbf{w}|\mathbf{a}; \zeta)} [\|f_{\tau, \mathbf{a}}^\zeta(\mathbf{w}) - h_{\tau, \mathbf{a}}^\xi(\mathbf{w})\|_2^2]. \quad (5)$$

However, similar to the FM objective, we do not have access to the true vector field  $f_{\tau, \mathbf{a}}^\zeta$  that induces the conditional probability path  $q_\tau(\mathbf{w}|\mathbf{a}; \zeta)$  with  $q_1(\mathbf{w}|\mathbf{a}; \zeta) \approx p(\mathbf{w}|\mathbf{a})$ . Following [35], we can introduce a latent random variable formulation to define the marginal probability path as

$$q_\tau(\mathbf{w}|\mathbf{a}; \zeta) = \int q_\tau(\mathbf{w}|\mathbf{a}, \mathbf{z}; \zeta) q(\mathbf{z}) d\mathbf{z},$$

where  $q_\tau(\mathbf{w}|\mathbf{a}, \mathbf{z}; \zeta)$  is the conditional probability path induced by the vector field  $\tilde{f}_{\tau, \mathbf{a}, \mathbf{z}}^\zeta : \mathbb{R}^{d_w} \rightarrow \mathbb{R}^{d_w}$  that acts as  $(\mathbf{w}) \mapsto \tilde{f}_{\tau, \mathbf{a}, \mathbf{z}}^\zeta(\mathbf{w})$  for each  $\mathbf{z} \in \mathbb{R}^{d_z}$ . Thus, we can define the vector field  $f_{\tau, \mathbf{a}}^\zeta$  as

$$f_{\tau, \mathbf{a}}^\zeta \triangleq \mathbb{E}_{q(\mathbf{z})} \left[ \frac{\tilde{f}_{\tau, \mathbf{a}, \mathbf{z}}^\zeta q_\tau(\mathbf{w}|\mathbf{a}, \mathbf{z}; \zeta)}{q_\tau(\mathbf{w}|\mathbf{a}; \zeta)} \right],$$

that will induce the conditional probability path  $q_\tau(\mathbf{w}|\mathbf{a}; \zeta)$ . We formalize this in the following theorem

**Theorem 1** (Finite-dimensional marginal vector field). *Given the vector field  $\tilde{f}_{\tau, \mathbf{a}, \mathbf{z}}^\zeta$  induces the conditional probability path  $q_\tau(\mathbf{w}|\mathbf{a}, \mathbf{z}; \zeta)$  with  $\mathbf{a} \sim p(\mathbf{a})$ ,  $\mathbf{z} \sim q(\mathbf{z})$  and  $\zeta \in \mathbb{R}^{n_\zeta}$ , then the vector field  $f_{\tau, \mathbf{a}}^\zeta$  defined as*

$$f_{\tau, \mathbf{a}}^\zeta \triangleq \mathbb{E}_{q(\mathbf{z})} \left[ \frac{\tilde{f}_{\tau, \mathbf{a}, \mathbf{z}}^\zeta q_\tau(\mathbf{w}|\mathbf{a}, \mathbf{z}; \zeta)}{q_\tau(\mathbf{w}|\mathbf{a}; \zeta)} \right],$$

induces the probability path  $q_\tau(\mathbf{w}|\mathbf{a}; \zeta)$ .

*Proof.* See Appendix B □

We can now define a tractable unbiased objective for learning the vector field  $h_{\tau, \mathbf{a}}^\xi$  as

$$J_{\text{PDE-CFM}}(\zeta, \xi) \triangleq \mathbb{E}_{\tau \sim \mathcal{U}[0,1], \mathbf{a} \sim p(\mathbf{a}), \mathbf{z} \sim q(\mathbf{z}), \mathbf{w} \sim q_\tau(\mathbf{w}|\mathbf{a}, \mathbf{z}; \zeta)} \left[ \left\| \gamma_\tau \left( \tilde{f}_{\tau, \mathbf{a}, \mathbf{z}}^\zeta(\mathbf{w}) - h_{\tau, \mathbf{a}}^\xi(\mathbf{w}) \right) \right\|_2^2 \right], \quad (6)$$

where  $\gamma_\tau \triangleq (1 + 2\tau^2)$  is a time-dependent scaling. Minimizing eq. (6) is equivalent to minimizing eq. (5) as formalized in the following theorem

**Theorem 2** (Finite-dimensional marginal vector field estimator). *Given the vector field  $\tilde{f}_{\tau, \mathbf{a}, \mathbf{z}}^\zeta$  induces the conditional probability path  $q_\tau(\mathbf{w}|\mathbf{a}, \mathbf{z}; \zeta)$  with  $\mathbf{a} \sim p(\mathbf{a})$ ,  $\mathbf{z} \sim q(\mathbf{z})$  and  $\zeta \in \mathbb{R}^{n_\zeta}$ , then up to a constant that is independent of trainable parameters  $\xi \in \mathbb{R}^{n_\xi}$  of the vector field  $h_{\tau, \mathbf{a}}^\xi$*

$$\arg \min_{\xi} J_{\text{PDE-FM}}(\zeta, \xi) = \arg \min_{\xi} J_{\text{PDE-CFM}}(\zeta, \xi).$$

*Proof.* See Appendix B □

Here, we introduce a time-dependent deterministic scaling  $\gamma_\tau$  to regularize the vector field in the limit  $\tau \rightarrow 1$ , emphasizing learning the vector field near the data distribution. To tractably sample from the conditional probability path  $q_\tau(\mathbf{w}|\mathbf{a}, \mathbf{z}; \zeta)$ , we need to design the latent distribution  $q(\mathbf{z})$  and the conditional probability path  $q_\tau(\mathbf{w}|\mathbf{a}, \mathbf{z}; \zeta)$  such that we can easily sample from them and compute the vector field  $\tilde{f}_{\tau, \mathbf{a}, \mathbf{z}}^\zeta$ . Specifically, we model the latent distribution as a joint distribution  $q(\mathbf{z}) = \pi(\mathbf{w})p(\mathbf{w}|\mathbf{a})$  between the prior and the conditional data distribution. As a result, we can model the conditional probability path as a transport of a Gaussian distribution with sample-dependent noise given as

$$\begin{aligned} q_\tau(\mathbf{w}|\mathbf{a}, \mathbf{z}; \zeta) &= \mathcal{N}(\mathbf{w}; \mu_\tau(\mathbf{z}), \sigma_\tau(\mathbf{z}; \zeta)), \\ \mu_\tau(\mathbf{z}) &\triangleq \tau \mathbf{w}_1 + (1 - \tau) \mathbf{w}_0, \quad \mathbf{w}_0 \sim \pi(\mathbf{w}), \mathbf{w}_1 \sim p(\mathbf{w}|\mathbf{a}), \\ \sigma_\tau(\mathbf{z}; \zeta) &\triangleq \sigma_{\min} \|\mathbf{w}_1 - \mathbf{w}_0\|_2^2. \end{aligned}$$

that results in the vector field  $\tilde{f}_{\tau, \mathbf{a}, \mathbf{z}}^\zeta = \mathbf{w}_1 - \mathbf{w}_0$  using eq. (4). Here, we introduce a sample-dependent noise to ensure high signal-to-noise ratio when the samples  $\mathbf{w}_0$  and  $\mathbf{w}_1$  are close to each other in  $\|\cdot\|_2$  sense.

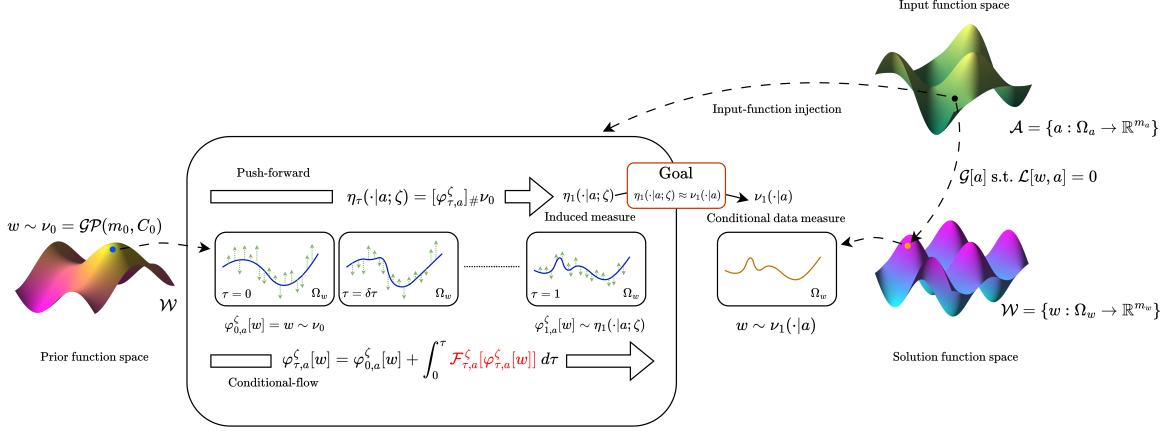


Figure 1: Schematic of operator view of flow-matching for PDE solution generation. Here, the vector field operator  $\mathcal{F}_{\tau,a}^\zeta$  induces a probability measure  $\nu_1(\cdot|a; \zeta)$  that seeks to approximate the conditional data measure  $\nu_1(\cdot|a)$  that characterizes the PDE solution for  $a \sim \nu_a$ .

The finite-dimensional view of solving the forward problem via flow-matching provides a framework for generating discretized PDE solutions that naturally incorporate predictive uncertainty. Instead of framing the forward problem as a deterministic regression over the PDE solution space, we reformulate it as learning the vector field  $h_{\tau,a}^\zeta$  that seeks to induce the conditional probability path  $q_\tau(\mathbf{w}|a; \zeta)$  such that  $q_1(\mathbf{w}|a; \zeta)$  models the conditional distribution  $p(\mathbf{w}|a)$ . Unlike traditional PINNs and neural operators, which yield a single deterministic solution, flow-matching characterizes the entire conditional distribution of solutions through the learned vector field  $h_{\tau,a}^\zeta$ . This directly integrates uncertainty quantification into the solution process, making the model inherently probabilistic rather than post hoc.

### 3.2. Operator view of generating PDE solutions with uncertainty quantification

In the finite-dimensional view of solving the forward problem using flow-matching, the input and solution domains  $\Omega_a$  and  $\Omega_w$  are discretized using a fixed evaluation operator  $\mathcal{E}_a^{n_a}$  and  $\mathcal{E}_w^{n_w}$ . This makes the forward problem tractable; however, it also restricts the PDE solution to be available only at push-forwards characterized by the fixed evaluation operators. This limits the generalizability of the learned model across the solution and input domains  $\Omega_w$  and  $\Omega_a$ , respectively, requiring retraining or ad hoc interpolation methods to learn across varying solution resolutions. In this section, we present a probabilistic operator view for generating PDE solutions, extending previous work [49, 50] to solve the forward problem in a conditional setting.

The key idea to obtain a probabilistic operator view for flow-matching for PDE solution generation is to model the vector fields as an operator defined on the product space  $\mathcal{W} \times \mathcal{A}$ , as illustrated in fig. 1. Consider the measurable spaces  $(\mathcal{W}, \mathcal{B}(\mathcal{W}))$  and  $(\mathcal{A}, \mathcal{B}(\mathcal{A}))$  for real and separable Hilbert spaces  $\mathcal{W}$  and  $\mathcal{A}$ , respectively, where  $\mathcal{B}(\cdot)$  denotes the Borel  $\sigma$ -algebra. Let  $\nu_a$  be the marginal probability measure defined on  $\mathcal{B}(\mathcal{A})$  for the input function  $a \in \mathcal{A}$ . We can define a joint data probability measure  $\nu_1$  on the measure space  $(\mathcal{W} \times \mathcal{A}, \mathcal{B}(\mathcal{W}) \otimes \mathcal{B}(\mathcal{A}))$  that disintegrates as  $\nu_1(dw, da) = \nu_1(dw|a)\nu_a(da)$  for each  $a \in \mathcal{A}$ , where  $\nu_1(\cdot|a)$  is a conditional probability measure defined in  $\mathcal{B}(\mathcal{W})$ . The marginal data probability measure is then given as  $\nu_1(X) = \nu_1(X \times \mathcal{A})$  for all  $X \in \mathcal{B}(\mathcal{W})$ . Consider a prior probability measure  $\nu_0$  defined in the measurable space  $(\mathcal{W}, \mathcal{B}(\mathcal{W}))$  for the PDE solution. Specifically, we can choose  $\nu_0$  as a Gaussian measure  $\mathcal{GP}(m_0, C_0)$  with mean function  $m_0 : \Omega_w \rightarrow \mathbb{R}^{m_w}$  and trace-class covariance operator  $C_0 : \mathcal{W} \rightarrow \mathcal{W}$  for which the absolute continuity is well known [54, 50]. Let  $\varphi^\zeta : [0, 1] \times \mathcal{W} \times \mathcal{A} \rightarrow \mathcal{W}$  be a parameterized, time-dependent diffeomorphic conditional flow that acts as  $(\tau, w, a) \mapsto \varphi_{\tau,a}^\zeta[w]$ , where  $\varphi_{\tau,a}^\zeta : \mathcal{W} \rightarrow \mathcal{W}$ . Given a smooth time-varying vector field operator  $\mathcal{F}^\zeta : [0, 1] \times \mathcal{W} \times \mathcal{A} \rightarrow \mathcal{W}$  that acts as  $(\tau, w, a) \mapsto \mathcal{F}_{\tau,a}^\zeta[w]$ , where  $\mathcal{F}_{\tau,a}^\zeta : \mathcal{W} \rightarrow \mathcal{W}$ , we can define a continuous transformation

between functions via the conditional ODE

$$\begin{aligned} \frac{d}{d\tau} \varphi_{\tau,a}^\zeta[w] &= \mathcal{F}_{\tau,a}^\zeta[\varphi_{\tau,a}^\zeta[w]], \quad \tau \in [0, 1], \\ \varphi_{0,a}^\zeta[w] &= w \sim \nu_0. \end{aligned}$$

As a result, the conditional flow induces a push-forward of the prior measure  $\nu_0$  given as  $\eta_\tau(\cdot|a; \zeta) \triangleq [\varphi_{\tau,a}^\zeta]_{\#} \nu_0$  that defines a time-varying conditional probability measure path with  $\eta_0(\cdot|a; \zeta) = \nu_0$  for each  $a \in \mathcal{A}$ . Similar to the finite-dimensional setting, we seek a vector field operator  $\mathcal{F}_{\tau,a}^\zeta$  that induces a conditional probability measure path  $\eta_\tau(\cdot|a; \zeta)$  such that  $\eta_1(\cdot|a; \zeta) \approx \nu_1(\cdot|a)$  for all  $a \sim \nu_a$ .

Following [49], we can learn a parametric approximation  $\mathcal{H}_{\tau,a}^\xi : \mathcal{W} \rightarrow \mathcal{W}$  of the vector field operator  $\mathcal{F}_{\tau,a}^\zeta$  informed by the input function  $a \in \mathcal{A}$  with parameters  $\xi \in \mathbb{R}^{n_\xi}$  by minimizing the empirical loss

$$J_{\text{PDE-OFM}}(\zeta, \xi) \triangleq \mathbb{E}_{\tau \sim \mathcal{U}[0,1], a \sim \nu_a, w \sim \eta_\tau(\cdot|a; \zeta)} [\|\mathcal{F}_{\tau,a}^\zeta[w] - \mathcal{H}_{\tau,a}^\xi[w]\|_{\mathcal{W}}^2].$$

However, similar to the finite-dimensional setting, we do not have access to the true vector field operator  $\mathcal{F}_{\tau,a}^\zeta$  that induces the conditional probability measure path  $\eta_\tau(\cdot|a; \zeta)$  with  $\eta_1(\cdot|a; \zeta) \approx \nu_1(\cdot|a)$ .

Consider a conditional coupling  $\kappa(\cdot|a)$  defined on the product space  $\mathcal{W} \times \mathcal{W}$  for each  $a \in \mathcal{A}$  such that  $\kappa(X \times \mathcal{W}|a) = \nu_0(X)$  and  $\kappa(\mathcal{W} \times X|a) = \nu_1(X|a)$  for all  $X \in \mathcal{B}(\mathcal{W})$ . Similar to §3.1, we can model  $\kappa(\cdot|a)$  as an independent coupling  $\kappa(\cdot|a) = \nu_0(\cdot)\nu_1(\cdot|a)$ , such that a realization  $z \sim \kappa(\cdot|a)$  is given as  $z = \{w_0, w_1\}$ , where  $w_0 \sim \nu_0$  and  $w_1 \sim \nu_1(\cdot|a)$ . The conditional measure  $\nu_1(\cdot|a, z)$  is designed to approximate the Dirac measures  $\delta_{w_0}$  and  $\delta_{w_1}$  at  $\tau = 0$  and  $\tau = 1$ , respectively. Following [50], we can then define the probability path  $\nu_\tau(\cdot|a; \zeta)$  via the disintegration

$$\eta_\tau(X|a; \zeta) = \int_{\mathcal{W} \times \mathcal{W}} \eta_\tau(X|a, z; \zeta) \kappa(dz|a), \quad \forall X \in \mathcal{B}(\mathcal{W}), a \in \mathcal{A}.$$

As a result, we can define a vector field operator  $\mathcal{F}_{\tau,a}^\zeta$  using a smooth and sufficiently regular vector field  $\tilde{\mathcal{F}}_{\tau,a,z}^\zeta : \mathcal{W} \rightarrow \mathcal{W}$  with  $\int_0^1 \int_{\mathcal{A}} \int_{\mathcal{W} \times \mathcal{W}} \int_{\mathcal{W}} \|\tilde{\mathcal{F}}_{\tau,a,z}^\zeta[w]\|_{\mathcal{W}} \eta_\tau(dw|a, z; \zeta) \kappa(dz|a) \nu_a(da) d\tau < \infty$  that induces  $\eta_\tau(\cdot|a, z; \zeta)$  as

$$\mathcal{F}_{\tau,a}^\zeta \triangleq \int_{\mathcal{W} \times \mathcal{W}} \tilde{\mathcal{F}}_{\tau,a,z}^\zeta \frac{d\eta_\tau(\cdot|a, z; \zeta)}{d\eta_\tau(\cdot|a; \zeta)} \kappa(dz|a), \quad (7)$$

which extends [49, Theorem 1] to the conditional setting and with a input-function dependent coupling  $\kappa(\cdot|a)$ . Thus, we can now define a tractable unbiased objective for learning the vector field operator  $\mathcal{H}_{\tau,a}^\xi$  as

$$J_{\text{PDE-COFM}}(\zeta, \xi) \triangleq \mathbb{E}_{\tau \sim \mathcal{U}[0,1], a \sim \nu_a, z \sim \kappa(\cdot|a), w \sim \eta_\tau(\cdot|a, z; \zeta)} \left[ \left\| \gamma_\tau \left( \tilde{\mathcal{F}}_{\tau,a,z}^\zeta[w] - \mathcal{H}_{\tau,a}^\xi[w] \right) \right\|_{\mathcal{W}}^2 \right], \quad (8)$$

which results in the same minimizer as the original objective  $J_{\text{PDE-OFM}}(\zeta, \xi)$ . The equivalence between the learning objectives can be obtained similarly to the finite-dimensional setting where the vector field  $\mathcal{F}_{\tau,a}^\zeta$  is defined using eq. (7), and inner products are defined in the Hilbert space. Similar to the finite-dimensional setting, we can construct  $\eta_\tau(\cdot|a, z; \zeta)$  as a Gaussian measure  $\mathcal{GP}(\mu_\tau(z), C_\tau(z; \zeta))$  with mean function  $\mu_\tau : \Omega_w \rightarrow \mathbb{R}^{m_w}$  and trace-class covariance operator  $C_\tau : \mathcal{W} \rightarrow \mathcal{W}$  given as

$$\begin{aligned} \mu_\tau(z) &\triangleq (1 - \tau)w_0 + \tau w_1, \quad z = \{w_0, w_1\}, \\ C_\tau(z; \zeta) &\triangleq \sigma_\tau^2 C_0, \end{aligned}$$

which remains trace-class given a trace-class covariance operator  $C_0$  of the prior measure  $\nu_0$  and finite time-dependent scaling  $\sigma_\tau \in \mathbb{R}_{>0}$ . Specifically, we consider  $\sigma_\tau = \sigma_{\min} \|w_1 - w_0\|_{\mathcal{W}}$  to ensure high signal-to-noise ratio when the samples  $w_0$  and  $w_1$  are close to each other in  $\|\cdot\|_{\mathcal{W}}$  sense. For such a transformation of Gaussian measure, the vector field operator  $\tilde{\mathcal{F}}_{\tau,a,z}^\zeta$  is given as

$$\tilde{\mathcal{F}}_{\tau,a,z}^\zeta[w] = \frac{d\sigma_\tau(z; \zeta)}{d\tau} \frac{(w - \mu_\tau(z))}{\sigma_\tau(z)} + \frac{d\mu_\tau(z)}{d\tau},$$

as shown by [49]. As a result, we can obtain the vector field operator  $\mathcal{F}_{\tau,a,z}^\zeta = w_1 - w_0$ .

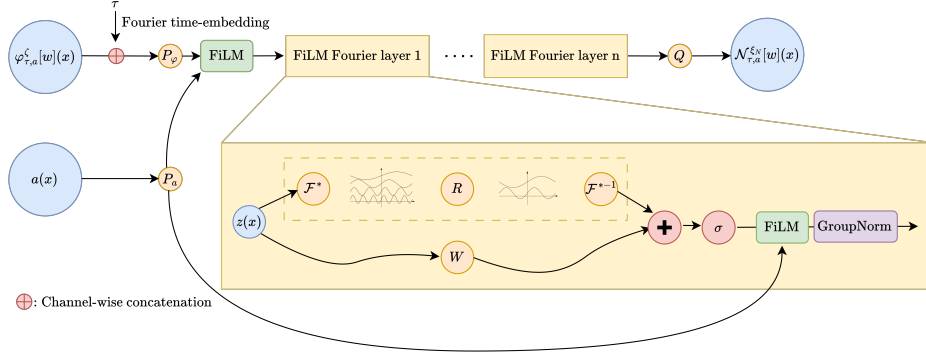


Figure 2: Schematic of the proposed FiLMFNO architecture for modeling the nonlinear operator  $\mathcal{N}_{\tau,a}^{\xi,N}$ . Here,  $P_\varphi$  and  $P_a$  are the projection operators that lift the inputs to a higher-dimensional channel space. After applying the FiLM Fourier layers composed of integral operators, activation functions, and FiLM layers for channel-wise modulation, the output is projected back to the target dimension by the operator  $Q$ . For the FiLM Fourier layers, first the input  $z$  is transformed to the Fourier space via the operator  $\mathcal{F}^*$ , followed by a linear transformation  $R$  to the lower Fourier modes, and lastly an inverse Fourier transform  $\mathcal{F}^{*-1}$ . The output of the inverse Fourier transform is added to a skip connection (after applying a local linear transformation  $W$ ), followed by nonlinear activation and FiLM conditioning.

*Modeling the vector field operator.* In this work, we decompose the model vector field operator into a linear and nonlinear (with respect to  $w$ ) components as

$$\mathcal{H}_{\tau,a}^\xi[w] = \mathcal{L}_{\tau,a}^{\xi,L}[w] + \mathcal{N}_{\tau,a}^{\xi,N}[w],$$

to improve model stability, as previously shown in the context of neural ordinary differential equations [55]. To model the linear operator, we can use linear convolution layers with a stride and kernel size 1 and no activation. For the nonlinear operator, we propose FiLMFNO, a conditional Fourier neural operator (FNO) [21] with feature-wise linear modulation (FiLM) [56] layers to effectively incorporate the input function  $a \in \mathcal{A}$  as conditioning information. The FiLM layers are effective in conditioning neural networks on auxiliary information across various domains. The proposed architecture is illustrated in fig. 2.

### 3.3. FLORAL: Flow-matching operator for residual-augmented learning of PDEs

Generating PDE solutions requires finite realizations  $\{(w_i, a_i)\}_{i=1}^\ell \sim \nu_1$  which can become prohibitively expensive to obtain, especially for complex, nonlinear PDEs. While flow-matching can be used to learn probabilistic operators, it typically requires a large number of training samples to accurately learn the vector field operator  $\mathcal{H}_{\tau,a}^\xi$ . To alleviate this data requirement, we propose FLORAL, a flow-matching operator for residual-augmented learning of PDEs that leverages low-fidelity data to enhance the data-efficiency of learning probabilistic operators via flow-matching.

Consider a low-fidelity solution operator  $\mathcal{G}_{\text{LF}} : \mathcal{A} \rightarrow \mathcal{W}$  that approximates the solution operator  $\mathcal{G} : \mathcal{A} \rightarrow \mathcal{W}$  such that

$$\mathcal{L}[\mathcal{G}_{\text{LF}}[a], a] \approx 0 \quad \forall a \in \mathcal{A}.$$

Often, such low-fidelity solution operators can be obtained inexpensively using simplified physics models, coarser discretizations, or surrogate models. While such low-fidelity operators provide valuable inductive biases, they often fail to accurately capture the true solution operator  $\mathcal{G}$  due to the underlying modeling assumptions.

To address this, we propose FLORAL, which incorporates useful inductive biases from the low-fidelity model and learns a residual correction to improve data efficiency. Specifically, FLORAL introduces a residual correction operator  $\mathcal{C} : \mathcal{A} \rightarrow \mathcal{W}$ , defined as

$$\mathcal{G}[a] = \mathcal{G}_{\text{LF}}[a] + \mathcal{C}[a] \quad \forall a \in \mathcal{A}, \quad (9)$$

where  $\mathcal{C}[a]$  seeks to correct the low-fidelity solution  $\mathcal{G}_{\text{LF}}[a]$  towards the high-fidelity solution manifold. While the correction operator may be functionally dependent on the known low-fidelity solution,

numerical experiments indicate that conditioning directly on the low-fidelity solution can marginally degrade model generalization. While both fidelities typically share the same input space  $\mathcal{A}$ , this assumption is not strict, and appropriate mappings can be employed to align differing input representations when necessary. The goal of FLORAL is then to learn a probabilistic model for the residual correction operator  $\mathcal{C}$  using flow-matching.

#### 4. Numerical Experiments

In this section, we demonstrate the performance of the proposed framework for learning probabilistic neural operators using multiple sources of information. To demonstrate the improvements in predictive performance enabled by multi-fidelity information, we also train a single-fidelity probabilistic neural operator, called FLORA, that uses only high-fidelity information. The functional datasets are designed to evaluate the framework’s capability to learn in the presence of multi-fidelity information, to handle non-linear correlations, and to manage a high-dimensional input feature space. For all numerical experiments, we consider a computationally efficient low-fidelity deterministic model with model-based errors. While the focus of this work is to demonstrate the benefits of multiple information sources for learning probabilistic neural operators, the framework can be extended to the case where a low-fidelity model is first learned in a supervised manner, then used to perform probabilistic multi-fidelity modeling. To quantify the performance of the proposed framework, we consider the root-mean-square error (RMSE), normalized RMSE (NRMSE), and conserved RMSE (CRMSE) metrics, as proposed in [57]. Since the goal is to improve the predictive performance, we also report the mean predictive error (mean  $L_2$  error) and the predictive uncertainty (mean standard deviation of the predictions). All numerical experiments and datasets used are provided in <https://github.com/sahilbhola14/floral> (available after acceptance).

##### 4.1. Artificial Benchmark 1: 1-dimensional problem with input function dependent correlation

Following [58], we consider a 1-dimensional problem where the correlation between the low- and high-fidelity functions is dependent on the input function  $a \in \mathcal{A} \triangleq \{a : \Omega_a \subset \mathbb{R} \rightarrow \mathbb{R}\}$ . The low-fidelity operator  $\mathcal{G}_{\text{LF}} : \mathcal{A} \rightarrow \mathcal{W}$ , where  $\mathcal{W} \triangleq \{w : \Omega_w \subset \mathbb{R} \rightarrow \mathbb{R}\}$  is given as

$$\mathcal{G}_{\text{LF}}[a](x) = \sin(a(x)) + x - 0.25a(x), \quad x \in \Omega_w,$$

and the high-fidelity operator  $\mathcal{G}_{\text{HF}} : \mathcal{A} \rightarrow \mathcal{W}$  is given as

$$\mathcal{G}_{\text{HF}}[a](x) = \sin(a(x)), \quad x \in \Omega_w, \tag{10}$$

with  $a(x) = kx - 4$ , where  $k \sim \mathcal{U}(10, 14)$ . Here, the input and solution functions are defined on the same domain, i.e.,  $\Omega_a = \Omega_w = [0, 1]$ , and  $x$  denotes the common spatial coordinate for both  $a$  and  $w$ . The goal is to learn a probabilistic operator  $\mathcal{G}^\theta : a \rightarrow w$  that can exploit the underlying correlation between the low- and high-fidelity functions.

For the high-fidelity and low-fidelity datasets, we first consider  $N_x = 128$  uniformly spaced spatial locations in  $\Omega_w$  and perform inference at the same resolution. Figure 3 illustrates samples of the generated high-fidelity function using FLORA and FLORAL along with the absolute error. Both flow-based models can generate high-fidelity function samples that closely match the true high-fidelity function, with the introduction of low-fidelity information reducing prediction uncertainty. Comparing the mean predictive error against the mean predictive uncertainty in fig. 4, we observe that FLORAL consistently outperforms FLORA across varying numbers of high-fidelity training samples, achieving lower predictive uncertainty for a given level of predictive error.

A key advantage of operator-based models is their ability to generalize to different discretizations. To demonstrate this, we consider training the model on a coarser spatial resolution of  $N_x = \{8, 16, 32, 64\}$  and perform inference on a finer resolution of 128 uniformly spaced domain points. Figure 5 illustrates samples of the generated high-fidelity function using FLORA and FLORAL along with the absolute error when trained with 8 spatial points. As shown, by leveraging the low-fidelity information, FLORAL can generate high-fidelity function samples that closely match the true high-fidelity function with high confidence, even when trained on a significantly coarser resolution. Quantitatively, fig. 6 shows that FLORAL consistently outperforms FLORA across training resolutions, achieving nearly an order-of-magnitude improvement in predictive accuracy for the  $16\times$  resolution increase.

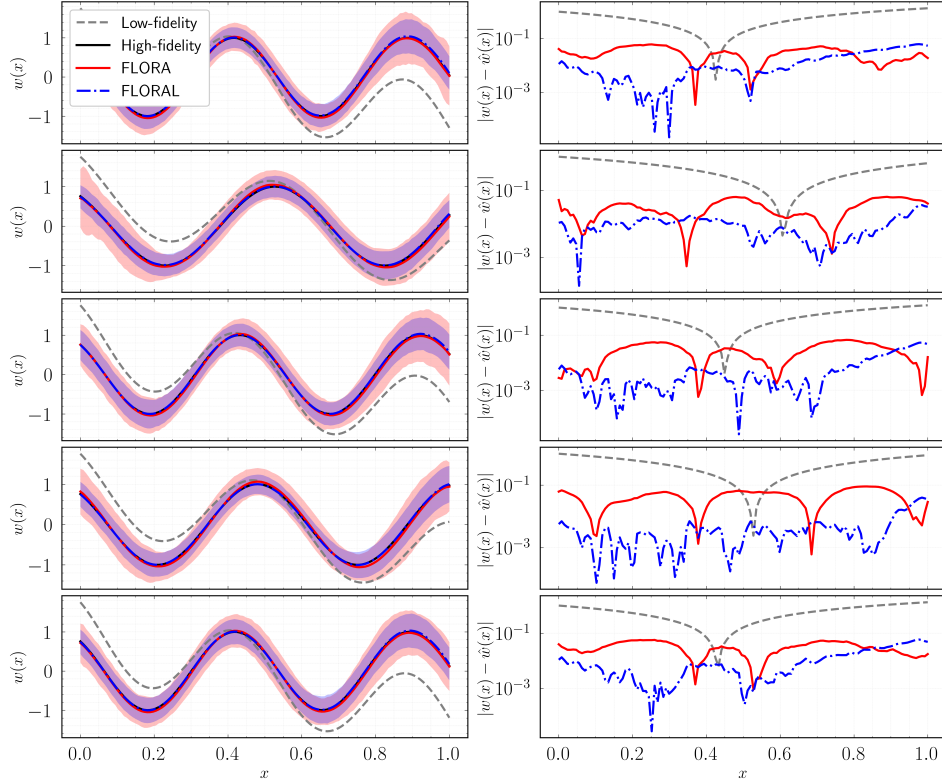


Figure 3: Samples of the generated high-fidelity function (left) using FLORA (—) and FLORAL (---) and the absolute error (right) for the 1-dimensional problem with input function correlation. The shaded region indicates  $\pm 10$  standard deviations about the mean for both models, computed using 100 generated ensembles. Model trained with 10 high-fidelity and corresponding low-fidelity training samples for a training and inference resolution of 128 discretization points.

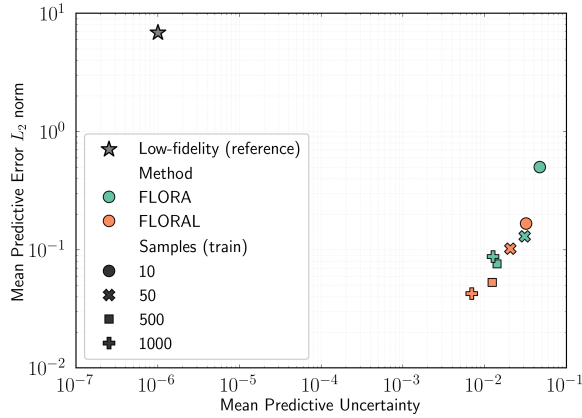


Figure 4: Mean predictive error vs. mean predictive uncertainty for varying number of training samples for the 1-dimensional problem with input function correlation. Predictive uncertainty is measured as the mean of the standard deviations of the generated samples. To compute the statistics, 1000 unseen high-fidelity function samples are used, and for each sample 100 ensembles are generated. Low-fidelity mean predictive uncertainty set to  $10^{-6}$  for visualization purposes only since the model is deterministic.

#### 4.2. 1-dimensional advection equation

We consider the 1-dimensional advection equation that models the transport of a conserved scalar field by a known velocity field. Mathematically, the 1-dimensional advection equation is described

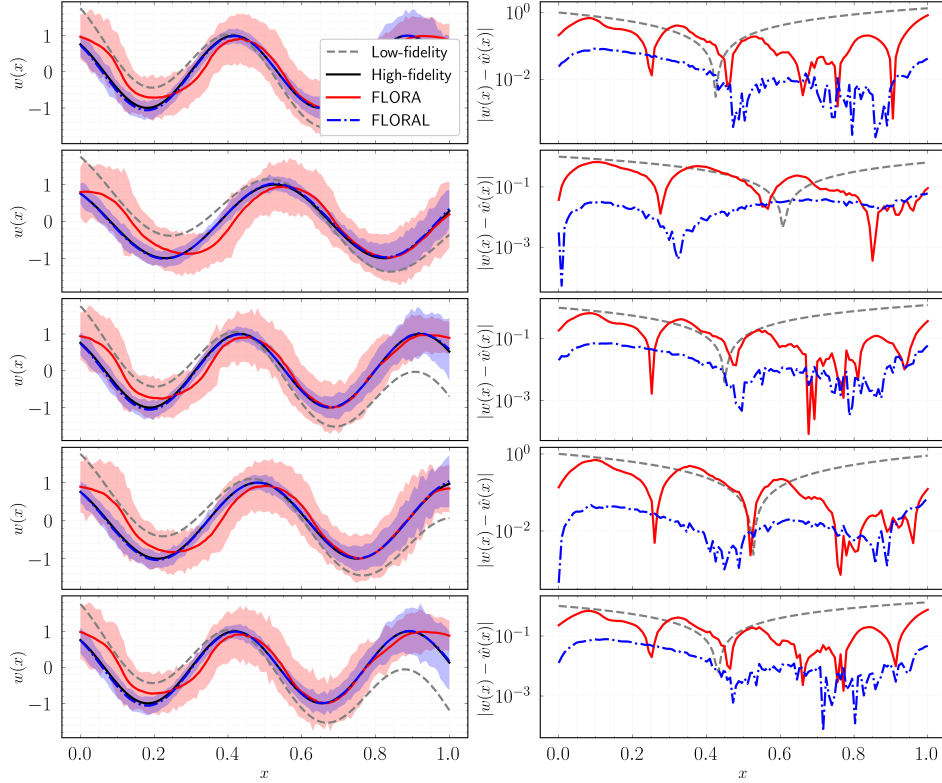


Figure 5: Samples of the generated high-fidelity function (left) using FLORA (—) and FLORAL (---) and the absolute error (right) for the 1-dimensional problem with input function correlation. The shaded region indicates  $\pm 10$  standard deviations about the mean for both models, computed using 100 generated ensembles. Model trained with 10 high-fidelity training samples using 8 discretization points, and inference is performed on 128 points, that is, a  $16\times$  resolution increase. Samples are generated on the same input function as in fig. 3.

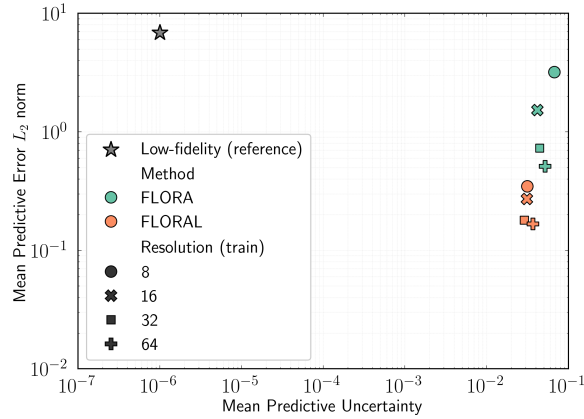


Figure 6: Mean predictive error vs. mean predictive uncertainty for varying training resolution for the 1-dimensional problem with input function correlation. Predictive uncertainty is measured as the mean of the standard deviations of the generated samples. Model trained with 10 high-fidelity training samples. To compute the statistics, 1000 unseen high-fidelity function samples are used, and for each sample 100 ensembles are generated. Low-fidelity mean predictive uncertainty is set to  $10^{-6}$  for visualization purposes only since the model is deterministic.

using the partial differential equation

$$\frac{\partial u(x, t)}{\partial t} + \beta \frac{\partial u(x, t)}{\partial x} = 0, \quad x \in [x_l, x_r], \quad t \in [0, T],$$

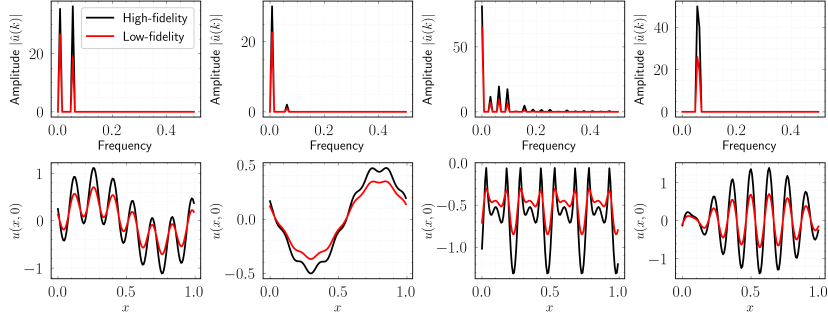


Figure 7: Comparison of high- (—) and low-fidelity (—) initial conditions in the spectral space (top row) and the corresponding physical space state (bottom row) for the 1-dimensional advection equation. The low-fidelity initial condition is obtained by applying a spectral filter, followed by amplitude distortion, to the high-fidelity initial condition to remove high-frequency components and introduce an amplitude bias.

where  $\beta$  is the constant advection velocity,  $u(x, 0)$  denotes the initial condition, and  $[x_l, x_r]$  is the spatial domain. Following [57], we consider  $x_l = 0$ ,  $x_r = 1$ ,  $T = 1$ , and a periodic boundary condition given as

$$u(x, 0) = \sum_{i=1}^N A_i \sin(k_i x + \phi_i), \quad x \in [0, 1], \quad (11)$$

where  $k_i = 2\pi n_i$  are the wave numbers with  $n_i \sim \mathcal{U}(\{1, \dots, n_{\max}\})$ . Here,  $N$  determines the number of superpositions of sine waves with random amplitudes  $A_i \sim \mathcal{U}(0, 1)$  and random phase shifts  $\phi_i \sim \mathcal{U}(0, 2\pi)$ . We set  $n_{\max} = 8$ ,  $N = 2$ , and  $\beta = 0.05$  for all the experiments. Similar to [57], after evaluating eq. (11), we apply an absolute value function, a random sign flip, and a window function with probabilities 0.1, 0.5, and 0.1, respectively. To obtain the numerical solution, we solve the advection equation using the first-order upwind finite-difference scheme and the forward Euler method for time integration.

To obtain the high-fidelity solution, we consider  $N_x = 128$  spatial grid points and  $N_t = 128$  temporal steps. We consider a low-fidelity solution on the same spatio-temporal grid; however, we introduce uncertainty in the initial condition to simulate model-form error. To construct the low-fidelity initial condition, we apply a spectral filter to the high-fidelity initial condition to remove high-frequency components and introduce amplitude distortion. Let  $\hat{u}_{\text{HF}}(k)$  for  $k = 0, \dots, K$  be the Fourier transform of the initial condition  $u(x, 0)$ , then the low-fidelity spectrum is constructed as

$$\hat{u}_{\text{LF}}(k) = s_A \hat{u}_{\text{HF}}(k) m_k \exp(-\gamma k/K),$$

where  $m_k$  retains only  $\max(2, \lfloor f_{\text{keep}} K \rfloor)$  Fourier modes,  $\exp(-\gamma k/K)$  introduces a mode-dependent amplitude damping, and  $s_A$  scales the amplitude. We consider  $f_{\text{keep}} = 0.4$ ,  $\gamma = 4$ , and  $s_A = 0.8$  for all the experiments. The low-fidelity initial condition is then obtained by applying the inverse Fourier transform to  $\hat{u}_{\text{LF}}(k)$ . An illustration of the high- and low-fidelity initial conditions is shown in fig. 7. The goal is to learn a probabilistic operator  $\mathcal{G}^\theta : u(x, 0) \rightarrow u(x, t)$  for all  $t \in [0, T]$  that can accurately predict the high-fidelity solution given the low-fidelity solution.

Figure 8 illustrates the absolute error in the solution obtained using the low-fidelity model, FLORA, and FLORAL on unseen initial conditions when trained with 500 high-fidelity training samples. Qualitatively, both probabilistic models can predict the high-fidelity solution with high accuracy. Figure 9 shows the RMSE, NRMSE, and CRMSE metrics of the proposed multi-fidelity probabilistic neural operator framework against single-fidelity baselines. As shown, introducing a low-fidelity source of information improves the predictive accuracy of the learned operator across all metrics. Furthermore, as shown in fig. 10, the proposed multi-fidelity framework achieves higher predictive accuracy for a given level of predictive uncertainty than the single-fidelity baselines.

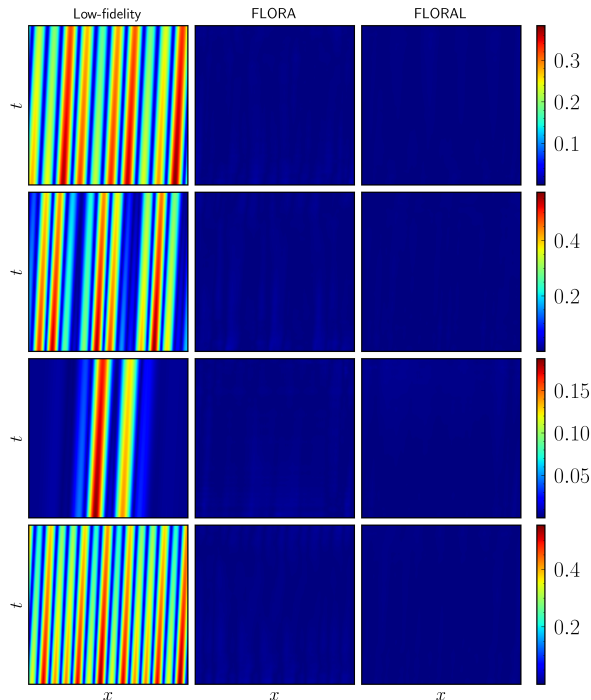


Figure 8: Illustration of absolute error in the solution obtained using low-fidelity model (left), FLORA (center), and FLORAL (right) on unseen initial conditions for the 1-dimensional advection equation. Model trained with 500 high-fidelity and corresponding low-fidelity training samples. To compute the mean prediction for probabilistic models, 50 ensembles are generated for each unseen initial condition.

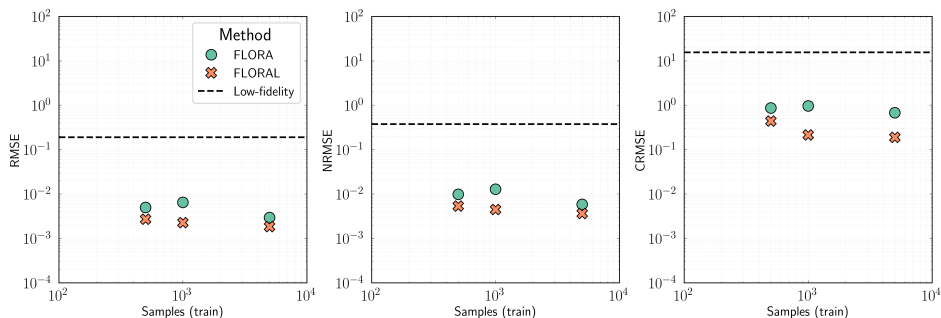


Figure 9: Comparison of RMSE (left), NRMSE (center), and CRMSE (right) for the 1-dimensional advection equation. To compute the statistics, 1000 unseen high-fidelity function samples are used, and for each sample, 50 ensembles are generated for the probabilistic models.

#### 4.3. 1-dimensional viscous Burgers' equation

We consider the 1-dimensional viscous Burgers' equation, a hyperbolic partial differential equation regularized by a diffusive term,

$$\frac{\partial u(x, t)}{\partial t} + u(x, t) \frac{\partial u(x, t)}{\partial x} = \nu \frac{\partial^2 u(x, t)}{\partial x^2}, \quad x \in [x_l, x_r], t \in [0, T],$$

which models the nonlinear advection-diffusion process in fluid dynamics. Here,  $\nu$  is the viscosity coefficient, which is assumed to be constant. We consider  $\nu = 0.01$ ,  $x_l = 0$ ,  $x_r = 1$ , and  $T = 0.2$  for all our experiments. Numerical solution is obtained by using a second-order upwind finite-difference scheme for the advection terms, a second-order central finite-difference scheme for the diffusion term, and a third-order strong stability preserving Runge-Kutta scheme for time integration.

To obtain the high-fidelity solution, we consider  $N_{x,\text{HF}} = 128$  spatial grid points and  $N_{t,\text{HF}} = 128$  temporal steps. We consider an initial condition for the high- and low-fidelity models similar to §4.2 with  $f_{\text{keep}} = 0.6$ . However, we further introduce discretization error in the low-fidelity model by

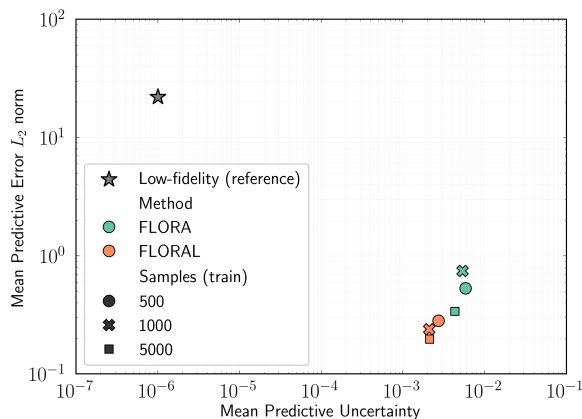


Figure 10: Mean predictive error vs. mean predictive uncertainty for varying number of training samples for the 1-dimensional advection equation. Predictive uncertainty is measured as the mean of the standard deviations of the generated samples. To compute the statistics, 1000 unseen high-fidelity function samples are used, and for each sample, 50 ensembles are generated for the probabilistic models. Low-fidelity mean predictive uncertainty is set to  $10^{-6}$  for visualization purposes only since the model is deterministic.

considering a coarser spatio-temporal resolution with  $N_{x;LF} = 64$  spatial grid points and  $N_{t;LF} = 64$  temporal steps. The goal is to learn a probabilistic operator  $\mathcal{G}^\theta : u(x, 0) \rightarrow u(x, t)$  for all  $t \in [0, T]$  that can accurately predict the high-fidelity solution given the low-fidelity solution.

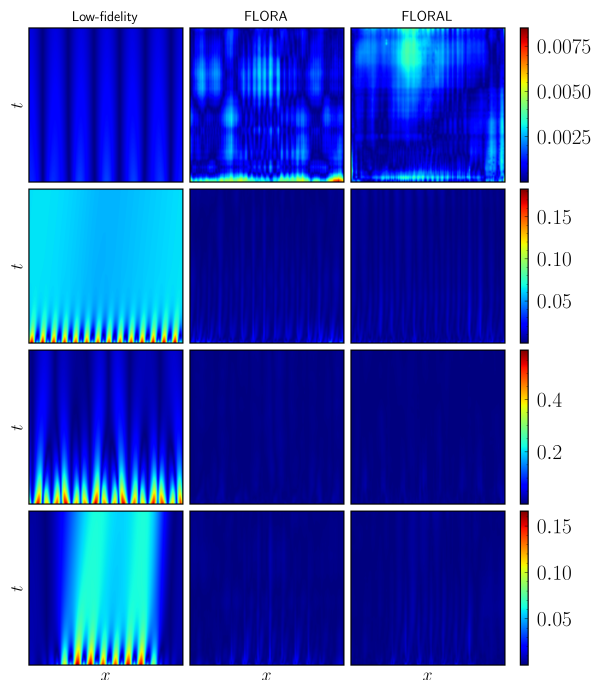


Figure 11: Illustration of absolute error in the solution obtained using low-fidelity model (left), FLORA (center), and FLORAL (right) on unseen initial conditions for the 1-dimensional Burgers' equation. Model trained with 500 high-fidelity training samples and corresponding low-fidelity training samples. To compute the mean prediction for probabilistic models, 50 ensembles are generated for each unseen initial condition.

Figure 11 illustrates the absolute error in the solution obtained using the low-fidelity model, FLORA, and FLORAL on unseen initial conditions when trained with 500 high-fidelity training samples. As shown, both probabilistic modeling approaches can generate samples with high predictive accuracy, with the case of leveraging low-fidelity information producing samples with qualitatively lower absolute errors. Quantitatively, fig. 12 illustrates the predictive performance, measured using various error metrics, of the proposed multi-fidelity operator learning against single-fidelity baselines. Across all metrics, introducing a low-fidelity source of information improves the predictive accuracy of the learned

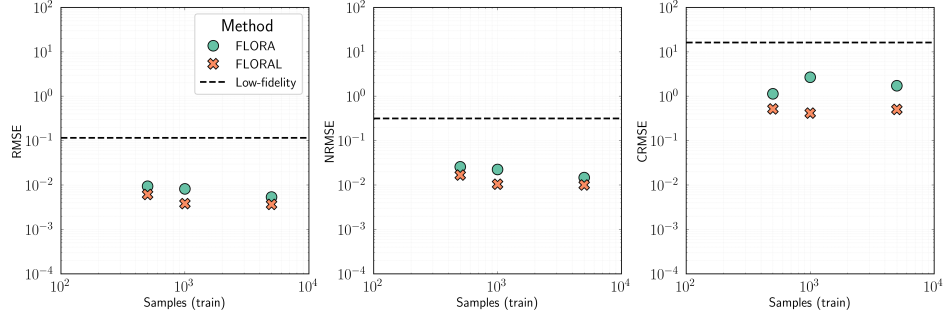


Figure 12: Comparison of RMSE (left), NRMSE (center), and CRMSE (right) for the 1-dimensional Burgers' equation. To compute the statistics, 1000 unseen high-fidelity function samples are used, and for each sample, 50 ensembles are generated for the probabilistic models.

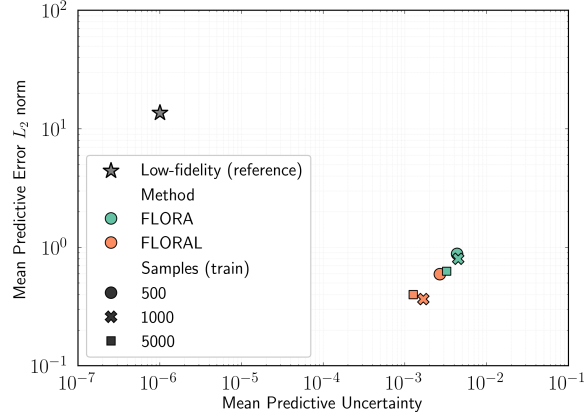


Figure 13: Mean predictive error vs. mean predictive uncertainty for varying number of training samples for the 1-dimensional Burgers' equation. Predictive uncertainty is measured as the mean of the standard deviations of the generated samples. To compute the statistics, 1000 unseen high-fidelity function samples are used, and for each sample, 50 ensembles are generated for the probabilistic models. Low-fidelity mean predictive uncertainty is set to  $10^{-6}$  for visualization purposes only since the model is deterministic.

operator. Further, as in §4.2, for any given level of predictive performance, we can improve predictive uncertainty by leveraging low-fidelity information, as shown in fig. 13.

#### 4.4. 2-dimensional Darcy Flow

We consider the two-dimensional Darcy flow problem, which relates the fluid pressure  $p(\mathbf{x})$  to the permeability  $K(\mathbf{x})$  of a porous medium. The permeability field specifies the degree to which the medium permits fluid flow at a spatial location  $\mathbf{x} \in \Omega \subset \mathbb{R}^2$ . The fluid pressure and velocity field  $\mathbf{u}(\mathbf{x})$  satisfy Darcy's law

$$\mathbf{u}(\mathbf{x}) = -K(\mathbf{x})\nabla p(\mathbf{x}), \quad \mathbf{x} \in \Omega, \quad (12a)$$

$$\nabla \cdot \mathbf{u}(\mathbf{x}) = f_s(\mathbf{x}), \quad \mathbf{x} \in \Omega, \quad (12b)$$

$$\mathbf{u}(\mathbf{x}) \cdot \hat{n}(\mathbf{x}) = 0, \quad \mathbf{x} \in \partial\Omega, \quad (12c)$$

$$\int_{\Omega} p(\mathbf{x}) d\mathbf{x} = 0, \quad (12d)$$

where  $\Omega = [0, 1]^2$  denotes the spatial domain and  $\partial\Omega = \{(x_1, x_2) \in \mathbb{R}^2 \mid x_1 \in \{0, 1\} \text{ or } x_2 \in \{0, 1\}\}$  denotes the boundary, with  $\hat{n}$  denoting the outward unit normal vector on  $\partial\Omega$ . Following [9, 41], we consider a source term  $f_s(\mathbf{x})$  to model an injection well on the left-bottom corner of  $\Omega$  and a production well in the right-top corner. Mathematically, the source term is defined as

$$f_s(\mathbf{x}) = \begin{cases} r, & \text{if } |x_i - \frac{1}{2}| \leq \frac{1}{2}s, \quad i = 1, 2, \\ -r, & \text{if } |x_i - (1 - \frac{1}{2}s)| \leq \frac{1}{2}s, \quad i = 1, 2, \\ 0, & \text{otherwise.} \end{cases}$$

where  $r$  is the rate of the wells and  $s$  is the size of the wells. The input log-permeability field is modeled as a Gaussian random field as  $K(\mathbf{x}) = \exp(G(\mathbf{x}))$ , where  $G(\mathbf{x})$  is a Gaussian process with a constant mean function  $\bar{\mu}$  and covariance function  $k(x, x') = \exp(-\|x - x'\|_2)/l$ . To solve the governing equations, we consider  $l = 0.1$ , kernel mean  $\bar{\mu} = 0$ , rate of the wells  $r = 50$ , and size of the wells  $s = 0.125$ . For dimensionality reduction, we limit the intrinsic dimensionality of the random permeability field by performing the Kosambi–Karhunen–Loève (KKL) expansion and retaining only the first  $q$  terms in

$$G(\mathbf{x}) = \bar{\mu} + \sum_{i=1}^q \sqrt{\lambda_i} \phi_i(\mathbf{x}) z_i,$$

where  $\lambda_i$  and  $\phi_i(\mathbf{x})$  are the  $i$ -th eigenvalue and eigenfunction of the covariance kernel  $k(x, x')$  sorted by decreasing  $\lambda_i$ , and  $z_i \sim \mathcal{N}(0, 1)$ . The resulting permeability field  $K(\mathbf{x})$  then deterministically defines the fluid pressure  $p(\mathbf{x})$  and velocity field  $\mathbf{u}(\mathbf{x})$ . After sampling  $K(\mathbf{x})$ , eq. (12d) is first solved for the pressure field, and then the velocity field is obtained using finite-difference approximation using the relation  $\mathbf{u}(\mathbf{x}) = -K(\mathbf{x})\nabla p(\mathbf{x})$ . To obtain the numerical solution, we follow the procedure in [41] where the finite-difference method with second-order central difference is used to approximate the first and second order spatial derivatives. To enforce the boundary condition for the fluid pressure, we use the Karush–Kuhn–Tucker conditions.

To generate the high- and low-fidelity datasets, we vary the intrinsic dimensionality  $q$  of the input permeability field  $K(\mathbf{x})$ . First, the high-fidelity dataset is generated by discretizing the computational domain into a uniform grid with  $N_{x_1;\text{HF}} = N_{x_2;\text{HF}} = 128$  points along each spatial direction, resulting in a total of  $N_{\text{HF}} = 128 \times 128$  grid points. To obtain the high-fidelity permeability fields, we consider  $q = 128$  terms in the KKL expansion. Following, we obtain the low-fidelity permeability fields by truncating the high-fidelity KKL expansion to  $q = 64$  terms. To introduce the discretization error in the low-fidelity model, we consider a coarser spatial resolution  $N_{x_1;\text{LF}} = N_{x_2;\text{LF}} = 32$  points along each spatial direction, resulting in a total of  $N_{\text{LF}} = 32 \times 32$  grid points. The goal is to learn a probabilistic operator  $\mathcal{G}^\theta : K(\mathbf{x}) \rightarrow p(\mathbf{x})$  that accurately predicts the high-fidelity solution given the low-fidelity solution. Figure 14 illustrates the absolute error in the predicted pressure field for unseen permeability

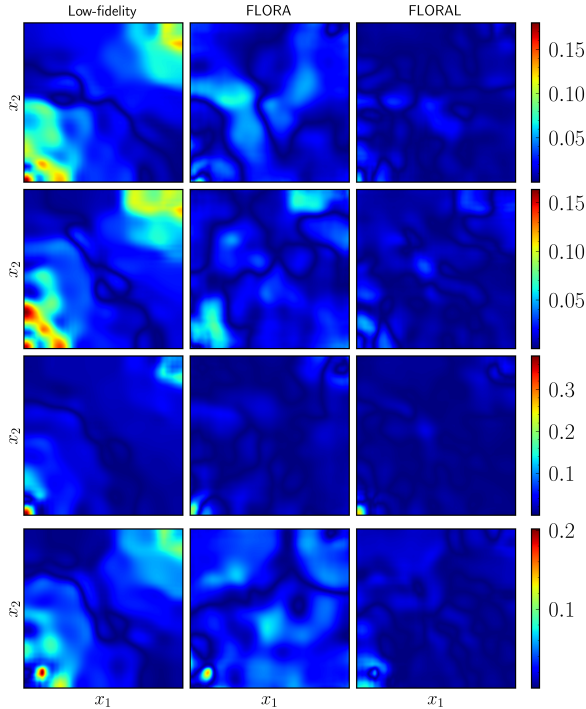


Figure 14: Illustration of absolute error in the solution obtained using low-fidelity model (left), FLORA (center), and FLORAL (right) on unseen permeability fields for the Darcy flow. Model trained with 500 high-fidelity training samples and corresponding low-fidelity training samples. To compute the mean prediction for probabilistic models, 50 ensembles are generated for each unseen permeability field.

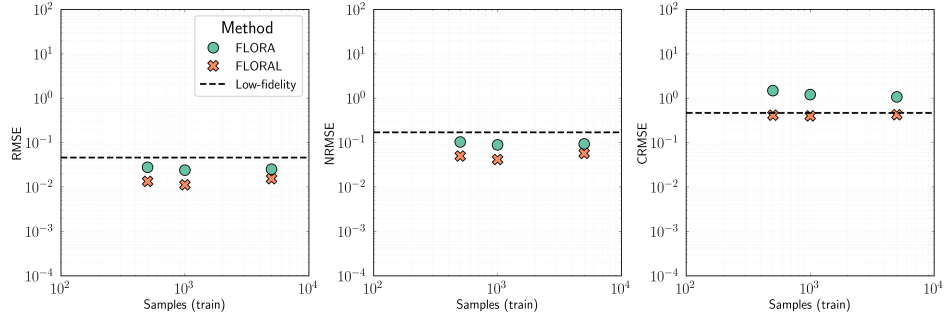


Figure 15: Comparison of RMSE (left), NRMSE (center), and CRMSE (right) for the Darcy flow. To compute the statistics, 1000 unseen high-fidelity function samples are used, and for each sample, 50 ensembles are generated for the probabilistic models.

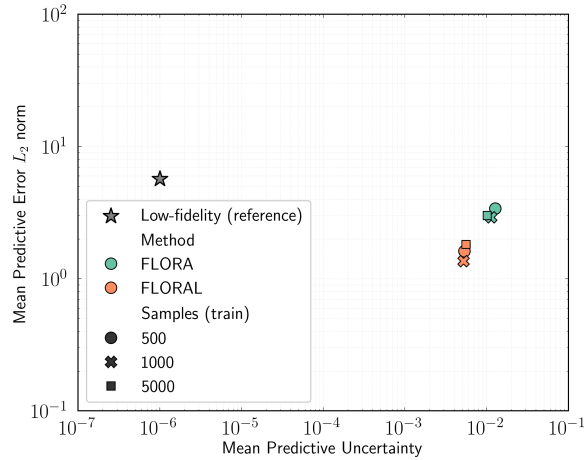


Figure 16: Mean predictive error vs. mean predictive uncertainty for varying number of training samples for the Darcy flow. Predictive uncertainty is measured as the mean of the standard deviations of the generated samples. To compute the statistics, 1000 unseen high-fidelity function samples are used, and for each sample, 50 ensembles are generated for the probabilistic models. Low-fidelity mean predictive uncertainty is set to  $10^{-6}$  for visualization purposes only since the model is deterministic.

fields using the low-fidelity model, FLORA, and FLORAL when trained with 500 high-fidelity training samples. Qualitatively, we can achieve lower absolute error in the mean prediction by leveraging the low-fidelity information. Comparing probabilistic operator models across all error metrics, leveraging low-fidelity information improves predictive accuracy. As shown in fig. 15, only considering single-fidelity information resulted in higher CRMSE compared to the low-fidelity model, and can be reduced by providing useful inductive bias through the low-fidelity model. Additionally, we can improve the mean predictive uncertainty for a given training set size by leveraging the low-fidelity information as shown in fig. 16.

## 5. Concluding remarks

In this work, we present FLORAL, a probabilistic framework for multi-fidelity neural operators that can effectively address the challenges of data scarcity, uncertainty quantification, and resolution dependence in scientific prediction. By formulating flow-matching generative modeling in a residual setting, FLORAL learns probabilistic corrections from low-fidelity surrogates to high-fidelity solutions, substantially improving data efficiency while providing principled uncertainty estimates through the learned flow map. This residual-augmented formulation reduces predictive variance and enables coherent probabilistic inference in data-limited regimes.

To support flexible inference at arbitrary resolution, we introduce a conditional neural operator architecture to model the vector field in the flow matching framework. This enables the inference of continuous-resolution solution operators, allowing users to query predictions at any desired discretiza-

tion level without retraining. We demonstrate the effectiveness of the proposed approach through numerical experiments on benchmark problems including the 1D advection equation, Burgers’ equation, and 2D Darcy flow. The following are key technical insights from this work:

- *Geometry of residual learning.* The consistent improvements from residual-augmented learning suggest that the correction manifold occupies a simpler region of function space than the full solution manifold. In the Darcy flow experiments, the single-fidelity probabilistic operator underperformed the deterministic low-fidelity model in RMSE, indicating that probabilistic modeling without appropriate inductive bias can be counterproductive. The low-fidelity model provides geometric structure that constrains the generative process to physically plausible regions.

- *Conditioning and generalization.* A subtle but consequential finding is that conditioning the flow on the input function rather than the low-fidelity solution yields better generalization. This suggests that the input space provides a more canonical representation for conditioning. The low-fidelity solution, while informative, introduces artifacts from its own approximation errors that can mislead the correction model.

- *Vector field regularization.* Two design choices proved essential for stable training. First, the time-dependent scaling  $\gamma_\tau = (1 + 2\tau^2)$  upweights the loss near  $\tau = 1$ , focusing learning capacity on the region where samples emerge. Second, the sample dependent noise  $\sigma_\tau \propto \|w_1 - w_0\|$  prevents signal collapse when the prior sample happens to be close to the target. The linear/nonlinear decomposition of the vector field operator further stabilizes training by isolating the smooth, large scale transport from the nonlinear corrections.

- *Resolution invariance.* The operator formulation’s ability to generalize across a  $16\times$  resolution gap is enabled by two factors: the trace-class covariance structure that ensures well-defined Gaussian measures in infinite dimensions, and the Fourier neural operator backbone that parameterizes resolution-independent spectral convolutions. Critically, this super-resolution capability degrades gracefully with the residual formulation but fails catastrophically for single-fidelity models, suggesting that the low-fidelity prior anchors the solution structure even when training data is extremely sparse.

- *Uncertainty quantification.* Unlike post-hoc approaches (dropout, ensembles, Laplace approximation) that impose uncertainty structure after training a deterministic model, flow matching directly learns the conditional distribution  $p(w|a)$ . The experiments reveal that this yields uncertainties that decrease appropriately as training data increases and that correlate spatially with regions of high solution complexity. The residual formulation further sharpens these estimates by removing the baseline variance already captured by the low-fidelity model.

**Limitations and future directions** The current framework assumes access to a low-fidelity model that shares the same input space as the high-fidelity target. Extending to settings with mismatched input representations, or learning the low-fidelity model jointly with the correction, remains open. The FiLM-FNO architecture, while effective, may not be optimal for all PDE classes. Investigating attention-based or graph-based operator backbones could expand applicability. Finally, the theoretical characterization of when residual learning provably reduces sample complexity, and by how much, could provide principled guidance for practitioners.

## Acknowledgements

This work was supported by the OUSD(RE) grant ‘*Physics-Aware Reduced Order Modeling for Nonequilibrium Plasma Flows*’ and by the Los Alamos National Laboratory grant ‘*Algorithm/Software/Hardware Co-design for High Energy Density applications*’.

## References

- [1] A. Quarteroni, A. Valli, Numerical approximation of partial differential equations, Springer, 1994.
- [2] P. Solín, Partial differential equations and the finite element method, John Wiley & Sons, 2005.
- [3] G. Carleo, I. Cirac, K. Cranmer, L. Daudet, M. Schuld, N. Tishby, L. Vogt-Maranto, L. Zdeborová, Machine learning and the physical sciences, Reviews of Modern Physics 91 (4) (2019) 045002.
- [4] S. L. Brunton, B. R. Noack, P. Koumoutsakos, Machine learning for fluid mechanics, Annual review of fluid mechanics 52 (1) (2020) 477–508.

- [5] S. L. Brunton, J. N. Kutz, Promising directions of machine learning for partial differential equations, *Nature Computational Science* 4 (7) (2024) 483–494.
- [6] G. E. Karniadakis, I. G. Kevrekidis, L. Lu, P. Perdikaris, S. Wang, L. Yang, Physics-informed machine learning, *Nature Reviews Physics* 3 (6) (2021) 422–440.
- [7] S. Cai, Z. Mao, Z. Wang, M. Yin, G. E. Karniadakis, Physics-informed neural networks (pinns) for fluid mechanics: A review, *Acta Mechanica Sinica* 37 (12) (2021) 1727–1738.
- [8] X. Guo, W. Li, F. Iorio, Convolutional neural networks for steady flow approximation, in: *Proceedings of the 22nd ACM SIGKDD international conference on knowledge discovery and data mining*, 2016, pp. 481–490.
- [9] Y. Zhu, N. Zabaras, Bayesian deep convolutional encoder–decoder networks for surrogate modeling and uncertainty quantification, *Journal of Computational Physics* 366 (2018) 415–447.
- [10] J. A. Weyn, D. R. Durran, R. Caruana, Can machines learn to predict weather? using deep learning to predict gridded 500-hpa geopotential height from historical weather data, *Journal of Advances in Modeling Earth Systems* 11 (8) (2019) 2680–2693.
- [11] S. Bhatnagar, Y. Afshar, S. Pan, K. Duraisamy, S. Kaushik, Prediction of aerodynamic flow fields using convolutional neural networks, *Computational Mechanics* 64 (2) (2019) 525–545.
- [12] Y. Khoo, J. Lu, L. Ying, Solving parametric pde problems with artificial neural networks, *European Journal of Applied Mathematics* 32 (3) (2021) 421–435.
- [13] W.-M. Lei, H.-B. Li, U-wno: U-net enhanced wavelet neural operator for solving parametric partial differential equations, *Computers & Mathematics with Applications* 194 (2025) 272–287.
- [14] S. Wiewel, M. Becher, N. Thuerey, Latent space physics: Towards learning the temporal evolution of fluid flow, in: *Computer graphics forum*, Vol. 38, Wiley Online Library, 2019, pp. 71–82.
- [15] K. Lee, K. T. Carlberg, Deep conservation: A latent-dynamics model for exact satisfaction of physical conservation laws, in: *Proceedings of the AAAI Conference on Artificial Intelligence*, Vol. 35, 2021, pp. 277–285.
- [16] M. G. Dissanayake, N. Phan-Thien, Neural-network-based approximations for solving partial differential equations, *communications in Numerical Methods in Engineering* 10 (3) (1994) 195–201.
- [17] I. E. Lagaris, A. Likas, D. I. Fotiadis, Artificial neural networks for solving ordinary and partial differential equations, *IEEE transactions on neural networks* 9 (5) (1998) 987–1000.
- [18] M. Raissi, P. Perdikaris, G. E. Karniadakis, Physics-informed neural networks: A deep learning framework for solving forward and inverse problems involving nonlinear partial differential equations, *Journal of Computational physics* 378 (2019) 686–707.
- [19] S. Hildebrand, S. Klinge, Comparison of neural fem and neural operator methods for applications in solid mechanics, *Neural Computing and Applications* 36 (27) (2024) 16657–16682.
- [20] L. Lu, P. Jin, G. Pang, Z. Zhang, G. E. Karniadakis, Learning nonlinear operators via deepnet based on the universal approximation theorem of operators, *Nature machine intelligence* 3 (3) (2021) 218–229.
- [21] Z. Li, N. Kovachki, K. Azizzadenesheli, B. Liu, K. Bhattacharya, A. Stuart, A. Anandkumar, Fourier neural operator for parametric partial differential equations, *arXiv preprint arXiv:2010.08895* (2020).
- [22] Z. Li, N. Kovachki, K. Azizzadenesheli, B. Liu, K. Bhattacharya, A. Stuart, A. Anandkumar, Neural operator: Graph kernel network for partial differential equations, *arXiv preprint arXiv:2003.03485* (2020).
- [23] L. Yang, X. Meng, G. E. Karniadakis, B-pinns: Bayesian physics-informed neural networks for forward and inverse pde problems with noisy data, *Journal of Computational Physics* 425 (2021) 109913.

- [24] Y. Gal, Z. Ghahramani, Dropout as a bayesian approximation: Representing model uncertainty in deep learning, in: international conference on machine learning, PMLR, 2016, pp. 1050–1059.
- [25] D. Zhang, L. Lu, L. Guo, G. E. Karniadakis, Quantifying total uncertainty in physics-informed neural networks for solving forward and inverse stochastic problems, *Journal of Computational Physics* 397 (2019) 108850.
- [26] I. Osband, Z. Wen, S. M. Asghari, V. Dwaracherla, M. Ibrahimi, X. Lu, B. Van Roy, Epistemic neural networks, *Advances in Neural Information Processing Systems* 36 (2023) 2795–2823.
- [27] A. S. Nair, B. Jacob, A. A. Howard, J. Drgona, P. Stinis, E-pinns: Epistemic physics-informed neural networks, *arXiv preprint arXiv:2503.19333* (2025).
- [28] E. Magnani, N. Krämer, R. Eschenhagen, L. Rosasco, P. Hennig, Approximate bayesian neural operators: Uncertainty quantification for parametric pdes, *arXiv preprint arXiv:2208.01565* (2022).
- [29] T. Weber, E. Magnani, M. Pförtner, P. Hennig, Uncertainty quantification for fourier neural operators, in: *ICLR 2024 workshop on AI4DifferentialEquations in science*, 2024.
- [30] I. J. Goodfellow, J. Pouget-Abadie, M. Mirza, B. Xu, D. Warde-Farley, S. Ozair, A. Courville, Y. Bengio, Generative adversarial nets, *Advances in neural information processing systems* 27 (2014).
- [31] A. Creswell, T. White, V. Dumoulin, K. Arulkumaran, B. Sengupta, A. A. Bharath, Generative adversarial networks: An overview, *IEEE signal processing magazine* 35 (1) (2018) 53–65.
- [32] J. Song, C. Meng, S. Ermon, Denoising diffusion implicit models, *arXiv preprint arXiv:2010.02502* (2020).
- [33] J. Ho, A. Jain, P. Abbeel, Denoising diffusion probabilistic models, *Advances in neural information processing systems* 33 (2020) 6840–6851.
- [34] Y. Lipman, R. T. Chen, H. Ben-Hamu, M. Nickel, M. Le, Flow matching for generative modeling, *arXiv preprint arXiv:2210.02747* (2022).
- [35] A. Tong, K. Fatras, N. Malkin, G. Huguet, Y. Zhang, J. Rector-Brooks, G. Wolf, Y. Bengio, Improving and generalizing flow-based generative models with minibatch optimal transport, *arXiv preprint arXiv:2302.00482* (2023).
- [36] G. Yang, S. Sommer, A denoising diffusion model for fluid field prediction, *arXiv preprint arXiv:2301.11661* (2023).
- [37] J. Huang, G. Yang, Z. Wang, J. J. Park, Diffusionpde: Generative pde-solving under partial observation, *Advances in Neural Information Processing Systems* 37 (2024) 130291–130323.
- [38] M. Lienen, D. Lüdke, J. Hansen-Palmus, S. Günemann, From zero to turbulence: Generative modeling for 3d flow simulation, 2024, URL <https://arxiv.org/abs/2306.01776>.
- [39] X.-Y. Liu, M. H. Parikh, X. Fan, P. Du, Q. Wang, Y.-F. Chen, J.-X. Wang, Conflid-inlet: Synthetic turbulence inflow using generative latent diffusion models with neural fields, *Physical Review Fluids* 10 (5) (2025) 054901.
- [40] L. Mosser, O. Dubrulle, M. J. Blunt, Reconstruction of three-dimensional porous media using generative adversarial neural networks, *Physical Review E* 96 (4) (2017) 043309.
- [41] C. Jacobsen, Y. Zhuang, K. Duraisamy, Cocogen: Physically consistent and conditioned score-based generative models for forward and inverse problems, *SIAM Journal on Scientific Computing* 47 (2) (2025) C399–C425.
- [42] L. Li, R. Carver, I. Lopez-Gomez, F. Sha, J. Anderson, Generative emulation of weather forecast ensembles with diffusion models, *Science Advances* 10 (13) (2024) eadk4489.

- [43] S. Fotiadis, N. Brenowitz, T. Geffner, Y. Cohen, M. Pritchard, A. Vahdat, M. Mardani, Stochastic flow matching for resolving small-scale physics, arXiv preprint arXiv:2410.19814 (2024).
- [44] M. A. Rahman, M. A. Florez, A. Anandkumar, Z. E. Ross, K. Azizzadenesheli, Generative adversarial neural operators, arXiv preprint arXiv:2205.03017 (2022).
- [45] G. Kerrigan, J. Ley, P. Smyth, Diffusion generative models in infinite dimensions, arXiv preprint arXiv:2212.00886 (2022).
- [46] J. Pidstrigach, Y. Marzouk, S. Reich, S. Wang, Infinite-dimensional diffusion models, arXiv preprint arXiv:2302.10130 (2023).
- [47] J. H. Lim, N. B. Kovachki, R. Baptista, C. Beckham, K. Azizzadenesheli, J. Kossaifi, V. Voleti, J. Song, K. Kreis, J. Kautz, et al., Score-based diffusion models in function space, *Journal of Machine Learning Research* 26 (158) (2025) 1–62.
- [48] J. Yao, A. Mammadov, J. Berner, G. Kerrigan, J. C. Ye, K. Azizzadenesheli, A. Anandkumar, Guided diffusion sampling on function spaces with applications to pdes, arXiv preprint arXiv:2505.17004 (2025).
- [49] G. Kerrigan, G. Migliorini, P. Smyth, Functional flow matching, arXiv preprint arXiv:2305.17209 (2023).
- [50] Y. Shi, Z. E. Ross, D. Asimaki, K. Azizzadenesheli, Stochastic process learning via operator flow matching, arXiv preprint arXiv:2501.04126 (2025).
- [51] X. Hou, X. Huang, P. Perdikaris, Cfo: Learning continuous-time pde dynamics via flow-matched neural operators, arXiv preprint arXiv:2512.05297 (2025).
- [52] R. T. Chen, Y. Rubanova, J. Bettencourt, D. K. Duvenaud, Neural ordinary differential equations, *Advances in neural information processing systems* 31 (2018).
- [53] G. Papamakarios, E. Nalisnick, D. J. Rezende, S. Mohamed, B. Lakshminarayanan, Normalizing flows for probabilistic modeling and inference, *Journal of Machine Learning Research* 22 (57) (2021) 1–64.
- [54] V. I. Bogachev, *Gaussian measures*, no. 62, American Mathematical Soc., 1998.
- [55] A. J. Linot, J. W. Burby, Q. Tang, P. Balaprakash, M. D. Graham, R. Maulik, Stabilized neural ordinary differential equations for long-time forecasting of dynamical systems, *Journal of Computational Physics* 474 (2023) 111838.
- [56] E. Perez, F. Strub, H. De Vries, V. Dumoulin, A. Courville, Film: Visual reasoning with a general conditioning layer, in: *Proceedings of the AAAI conference on artificial intelligence*, Vol. 32, 2018.
- [57] M. Takamoto, T. Praditia, R. Leiteritz, D. MacKinlay, F. Alesiani, D. Pflüger, M. Niepert, Pdebench: An extensive benchmark for scientific machine learning, *Advances in Neural Information Processing Systems* 35 (2022) 1596–1611.
- [58] A. Thakur, T. Tripura, S. Chakraborty, Multi-fidelity wavelet neural operator with application to uncertainty quantification, arXiv preprint arXiv:2208.05606 (2022).
- [59] C. Villani, et al., *Optimal transport: old and new*, Vol. 338, Springer, 2008.
- [60] J. Gardner, G. Pleiss, K. Q. Weinberger, D. Bindel, A. G. Wilson, Gpytorch: Blackbox matrix-matrix gaussian process inference with gpu acceleration, *Advances in neural information processing systems* 31 (2018).
- [61] J. Kossaifi, N. Kovachki, Z. Li, D. Pitt, M. Liu-Schiaffini, V. Duruisseaux, R. J. George, B. Bonev, K. Azizzadenesheli, J. Berner, A. Anandkumar, A library for learning neural operators, arXiv preprint arXiv:2412.10354 (2025).

## Appendix A Continuity Equation

Any vector field  $u_\tau^\zeta : \mathbb{R}^{d_y} \rightarrow \mathbb{R}^{d_y}$  defined for  $\mathbf{y} \in \mathbb{R}^{d_y}$  induces the probability path  $q_\tau(\mathbf{y}; \zeta)$  if it satisfies the continuity equation

$$\frac{\partial q_\tau(\mathbf{y}; \zeta)}{\partial \tau} + \nabla \cdot (q_\tau(\mathbf{y}; \zeta) u_\tau^\zeta(\mathbf{y})) = 0,$$

where  $\nabla(\cdot)$  denotes the divergence operator [59]. The continuity equation is necessary and sufficient to ensure that the probability path  $q_\tau(\mathbf{y}; \zeta)$  evolves according to the flow characterized by the vector field  $u_\tau(\mathbf{y}; \zeta)$ .

## Appendix B Theorem Proofs

*Proof of theorem 1.* For any vector field to induce a probability path, it must satisfy the continuity condition (see Appendix A).

$$\begin{aligned} \frac{\partial q_\tau(\mathbf{w}|\mathbf{a}; \zeta)}{\partial \tau} &= \frac{\partial}{\partial \tau} \mathbb{E}_{q(\mathbf{z})} [q_\tau(\mathbf{w}|\mathbf{a}, \mathbf{z}; \zeta)], \\ &= \mathbb{E}_{q(\mathbf{z})} \left[ \frac{\partial q_\tau(\mathbf{w}|\mathbf{a}, \mathbf{z}; \zeta)}{\partial \tau} \right]. \end{aligned}$$

Given that  $\tilde{f}_{\tau, \mathbf{a}, \mathbf{z}}^\zeta$  induces the conditional probability path  $q_\tau(\mathbf{w}|\mathbf{a}, \mathbf{z}; \zeta)$ , we have

$$\begin{aligned} \frac{\partial q_\tau(\mathbf{w}|\mathbf{a}; \zeta)}{\partial \tau} &= -\mathbb{E}_{q(\mathbf{z})} \left[ \nabla \cdot \left( q_\tau(\mathbf{w}|\mathbf{a}, \mathbf{z}; \zeta) \tilde{f}_{\tau, \mathbf{a}, \mathbf{z}}^\zeta(\mathbf{w}) \right) \right], \\ &= -\nabla \cdot \left( \mathbb{E}_{q(\mathbf{z})} \left[ q_\tau(\mathbf{w}|\mathbf{a}, \mathbf{z}; \zeta) \tilde{f}_{\tau, \mathbf{a}, \mathbf{z}}^\zeta(\mathbf{w}) \right] \right), \\ &= -\nabla \cdot \left( \mathbb{E}_{q(\mathbf{z})} \left[ \frac{q_\tau(\mathbf{w}|\mathbf{a}, \mathbf{z}; \zeta) \tilde{f}_{\tau, \mathbf{a}, \mathbf{z}}^\zeta(\mathbf{w}) q_\tau(\mathbf{w}|\mathbf{a}; \zeta)}{q_\tau(\mathbf{w}|\mathbf{a}; \zeta)} \right] \right), \\ &= -\nabla \cdot \left( q_\tau(\mathbf{w}|\mathbf{a}; \zeta) \mathbb{E}_{q(\mathbf{z})} \left[ \frac{q_\tau(\mathbf{w}|\mathbf{a}, \mathbf{z}; \zeta) \tilde{f}_{\tau, \mathbf{a}, \mathbf{z}}^\zeta(\mathbf{w})}{q_\tau(\mathbf{w}|\mathbf{a}; \zeta)} \right] \right), \end{aligned}$$

where for  $f_{\tau, \mathbf{a}}^\zeta \triangleq \mathbb{E}_{q(\mathbf{z})} \left[ \frac{\tilde{f}_{\tau, \mathbf{a}, \mathbf{z}}^\zeta q_\tau(\mathbf{w}|\mathbf{a}, \mathbf{z}; \zeta)}{q_\tau(\mathbf{w}|\mathbf{a}; \zeta)} \right]$  we satisfy the continuity equation

$$\frac{\partial q_\tau(\mathbf{w}|\mathbf{a}; \zeta)}{\partial \tau} + \nabla \cdot (q_\tau(\mathbf{w}|\mathbf{a}; \zeta) f_{\tau, \mathbf{a}}^\zeta(\mathbf{w})) = 0.$$

□

*Proof of theorem 2.* Similar to [34, 35], we assume that the conditional probability path  $q_\tau(\mathbf{w}|\mathbf{a}; \zeta) > 0$  for the entire support of  $p(\mathbf{a})$ . To ensure the existence of all the involved integrals and changing of order, we assume that  $q(\mathbf{z})$ ,  $q(\mathbf{w}|\mathbf{a}, \mathbf{z}; \zeta)$  are decreasing to zero at sufficient speed as  $\|\mathbf{w}\| \rightarrow \infty$  for the entire support of  $p(\mathbf{a})$ . We assume that the vector fields  $f_{\tau, \mathbf{a}}^\zeta$ ,  $h_{\tau, \mathbf{a}}^\zeta$ , and  $\nabla_\xi h_{\tau, \mathbf{a}}^\zeta$  are bounded. Using the bi-linearity of inner products,

$$\begin{aligned} \|f_{\tau, \mathbf{a}}^\zeta(\mathbf{w}) - h_{\tau, \mathbf{a}}^\zeta(\mathbf{w})\|_2^2 &= \|f_{\tau, \mathbf{a}}^\zeta(\mathbf{w})\|_2^2 - 2 \langle f_{\tau, \mathbf{a}}^\zeta(\mathbf{w}), h_{\tau, \mathbf{a}}^\zeta(\mathbf{w}) \rangle + \|h_{\tau, \mathbf{a}}^\zeta(\mathbf{w})\|_2^2, \\ \left\| \gamma_\tau \left( \tilde{f}_{\tau, \mathbf{a}, \mathbf{z}}^\zeta(\mathbf{w}) - h_{\tau, \mathbf{a}}^\zeta(\mathbf{w}) \right) \right\|_2^2 &= \gamma_\tau^2 \left( \| \tilde{f}_{\tau, \mathbf{a}, \mathbf{z}}^\zeta(\mathbf{w}) \|_2^2 - 2 \langle \tilde{f}_{\tau, \mathbf{a}, \mathbf{z}}^\zeta(\mathbf{w}), h_{\tau, \mathbf{a}}^\zeta(\mathbf{w}) \rangle + \| h_{\tau, \mathbf{a}}^\zeta(\mathbf{w}) \|_2^2 \right). \end{aligned}$$

Using the marginalization property, we have

$$\mathbb{E}_{q_\tau(\mathbf{w}|\mathbf{a}; \zeta)} [\|h_{\tau, \mathbf{a}}^\zeta(\mathbf{w})\|_2^2] = \mathbb{E}_{q(\mathbf{z})} [\mathbb{E}_{q_\tau(\mathbf{w}|\mathbf{a}, \mathbf{z}; \zeta)} [\|h_{\tau, \mathbf{a}}^\zeta(\mathbf{w})\|_2^2]].$$

Now, using theorem 1 to define the vector field  $f_{\tau,\mathbf{a}}^\zeta$ , we have

$$\begin{aligned}
\mathbb{E}_{q_\tau(\mathbf{w}|\mathbf{a};\zeta)} [\langle f_{\tau,\mathbf{a}}^\zeta(\mathbf{w}), h_{\tau,\mathbf{a}}^\xi(\mathbf{w}) \rangle] &= \mathbb{E}_{q_\tau(\mathbf{w}|\mathbf{a};\zeta)} \left[ \left\langle \mathbb{E}_{q(\mathbf{z})} \left[ \frac{\tilde{f}_{\tau,\mathbf{a},\mathbf{z}}^\zeta(\mathbf{w}) q_\tau(\mathbf{w}|\mathbf{a},\mathbf{z};\zeta)}{q_\tau(\mathbf{w}|\mathbf{a};\zeta)} \right], h_{\tau,\mathbf{a}}^\xi(\mathbf{w}) \right\rangle \right], \\
&= \int q_\tau(\mathbf{w}|\mathbf{a};\zeta) \left\langle \int q(\mathbf{z}) \frac{\tilde{f}_{\tau,\mathbf{a},\mathbf{z}}^\zeta(\mathbf{w}) q_\tau(\mathbf{w}|\mathbf{a},\mathbf{z};\zeta)}{q_\tau(\mathbf{w}|\mathbf{a};\zeta)} d\mathbf{z}, h_{\tau,\mathbf{a}}^\xi(\mathbf{w}) \right\rangle d\mathbf{w}, \\
&= \int \left\langle \int q(\mathbf{z}) \tilde{f}_{\tau,\mathbf{a},\mathbf{z}}^\zeta(\mathbf{w}) q_\tau(\mathbf{w}|\mathbf{a},\mathbf{z};\zeta) d\mathbf{z}, h_{\tau,\mathbf{a}}^\xi(\mathbf{w}) \right\rangle d\mathbf{w}, \\
&= \int \int \left\langle q(\mathbf{z}) \tilde{f}_{\tau,\mathbf{a},\mathbf{z}}^\zeta(\mathbf{w}) q_\tau(\mathbf{w}|\mathbf{a},\mathbf{z};\zeta), h_{\tau,\mathbf{a}}^\xi(\mathbf{w}) \right\rangle d\mathbf{z} d\mathbf{w}, \\
&= \int \int q(\mathbf{z}) q_\tau(\mathbf{w}|\mathbf{a},\mathbf{z};\zeta) \left\langle \tilde{f}_{\tau,\mathbf{a},\mathbf{z}}^\zeta(\mathbf{w}), h_{\tau,\mathbf{a}}^\xi(\mathbf{w}) \right\rangle d\mathbf{z} d\mathbf{w}, \\
&= \mathbb{E}_{q(\mathbf{z})} \left[ \mathbb{E}_{q_\tau(\mathbf{w}|\mathbf{a},\mathbf{z};\zeta)} \left[ \left\langle \tilde{f}_{\tau,\mathbf{a},\mathbf{z}}^\zeta(\mathbf{w}), h_{\tau,\mathbf{a}}^\xi(\mathbf{w}) \right\rangle \right] \right].
\end{aligned}$$

Since  $\nabla_\xi \|f_{\tau,\mathbf{a}}^\zeta(\mathbf{w})\|_2^2 = 0$ , we have

$$\begin{aligned}
\nabla_\xi J_{\text{PDE-FM}}(\zeta, \xi) &= \mathbb{E}_{\tau \sim \mathcal{U}(0,1), p(\mathbf{a})} \left[ \nabla_\xi \mathbb{E}_{q_\tau(\mathbf{w}|\mathbf{a};\zeta)} \left[ \|f_{\tau,\mathbf{a}}^\zeta(\mathbf{w}) - h_{\tau,\mathbf{a}}^\xi(\mathbf{w})\|_2^2 \right] \right], \\
&= \mathbb{E}_{\tau \sim \mathcal{U}(0,1), p(\mathbf{a})} \left[ \nabla_\xi \mathbb{E}_{q(\mathbf{z})} \left[ \mathbb{E}_{q_\tau(\mathbf{w}|\mathbf{a},\mathbf{z};\zeta)} \left[ -2 \langle \tilde{f}_{\tau,\mathbf{a},\mathbf{z}}^\zeta(\mathbf{w}), h_{\tau,\mathbf{a}}^\xi(\mathbf{w}) \rangle + \|h_{\tau,\mathbf{a}}^\xi(\mathbf{w})\|_2^2 \right] \right] \right], \\
&= \mathbb{E}_{\tau \sim \mathcal{U}(0,1), p(\mathbf{a})} \left[ \nabla_\xi \mathbb{E}_{q(\mathbf{z}), q_\tau(\mathbf{w}|\mathbf{a},\mathbf{z};\zeta)} \left[ \left\| \tilde{f}_{\tau,\mathbf{a},\mathbf{z}}^\zeta(\mathbf{w}) - h_{\tau,\mathbf{a}}^\xi(\mathbf{w}) \right\|_2^2 \right] \right], \\
&= \mathbb{E}_{\tau \sim \mathcal{U}(0,1), p(\mathbf{a}), q(\mathbf{z}), q_\tau(\mathbf{w}|\mathbf{a},\mathbf{z};\zeta)} \left[ \nabla_\xi \left\| \tilde{f}_{\tau,\mathbf{a},\mathbf{z}}^\zeta(\mathbf{w}) - h_{\tau,\mathbf{a}}^\xi(\mathbf{w}) \right\|_2^2 \right], \\
&= \nabla_\xi \mathbb{E}_{\tau \sim \mathcal{U}(0,1), p(\mathbf{a}), q(\mathbf{z}), q_\tau(\mathbf{w}|\mathbf{a},\mathbf{z};\zeta)} \left[ \left\| \tilde{f}_{\tau,\mathbf{a},\mathbf{z}}^\zeta(\mathbf{w}) - h_{\tau,\mathbf{a}}^\xi(\mathbf{w}) \right\|_2^2 \right], \\
&\triangleq \nabla_\xi J_{\text{PDE-CFM}}^\dagger(\zeta, \xi),
\end{aligned}$$

where  $J_{\text{PDE-CFM}}^\dagger(\zeta, \xi) \triangleq \mathbb{E}_{\tau \sim \mathcal{U}(0,1)} \ell_{\text{PDE-CFM}}^\dagger$  with

$$\ell_{\text{PDE-CFM}}^\dagger \triangleq \mathbb{E}_{p(\mathbf{a}), q(\mathbf{z}), q_\tau(\mathbf{w}|\mathbf{a},\mathbf{z};\zeta)} \left[ \left\| \tilde{f}_{\tau,\mathbf{a},\mathbf{z}}^\zeta(\mathbf{w}) - h_{\tau,\mathbf{a}}^\xi(\mathbf{w}) \right\|_2^2 \right].$$

As a result, minimizing  $J_{\text{PDE-FM}}(\zeta, \xi)$  with respect to  $\xi$  is equivalent to minimizing  $J_{\text{PDE-CFM}}^\dagger(\zeta, \xi)$  with respect to  $\xi$ . Using the definition of  $J_{\text{PDE-CFM}}(\zeta, \xi)$  from eq. (6), we have

$$J_{\text{PDE-CFM}}(\zeta, \xi) = \mathbb{E}_{\tau \sim \mathcal{U}(0,1)} [\gamma_\tau^2 \ell_{\text{PDE-CFM}}^\dagger],$$

such that  $\nabla_\xi J_{\text{PDE-CFM}}(\zeta, \xi) = \mathbb{E}_{\tau \sim \mathcal{U}(0,1)} [\gamma_\tau^2 \nabla_\xi \ell_{\text{PDE-CFM}}^\dagger]$ . As a result,

$$\arg \min_\xi J_{\text{PDE-CFM}}(\zeta, \xi) = \arg \min_\xi J_{\text{PDE-CFM}}^\dagger(\zeta, \xi) = \arg \min_\xi J_{\text{PDE-FM}}(\zeta, \xi),$$

for  $\gamma_\tau > 0$  since it is a time-dependent constant that is independent of  $\xi$ .  $\square$

## Appendix C Additional results and details

This section contains additional details and results for the experiments presented in the main manuscript. For each experiment performed, we require samples from a Gaussian process measure. In our work, we consider a zero-mean (that is,  $m_0 = 0$ ) Gaussian process parameterized by a Matern covariance kernel with smoothness factor  $\nu = 0.5$  and length scale of  $10^{-3}$ . We implement this using the GPyTorch library [60]. To model the vector fields using an operator, we propose a conditional Fourier neural operator [21] leveraging feature-wise linear modulation (FiLM) [56], called FiLMFNO, using the `neuraloperator` library [61]. The hyperparameters for FiLMFNO have the same meaning as described in the `neuraloperator` library. For all experiments, we have considered 4 Fourier layers,

Table C1: Training configurations for the 1-dimensional problem with input function correlation. Both equal-resolution and multi-resolution settings are reported.

<b>Train→Infer Resolution</b>	<b>Epochs</b>	<b>Train Size</b>	<b>Validation Size</b>	<b>Batch Size</b>	<b># Fourier Modes</b>
128 → 128	300	10	1,000	2	64
		50		4	
		500		16	
		1,000		64	
8 → 128	300	10	1,000	2	4
16 → 128					8
32 → 128					16
64 → 128					32

64 hidden channels, 4 lifting channel ratio, and 4 projection channel ratio. To compute the coefficients of the FiLM layers, we use fully connected neural networks with 3 hidden layers of 64 neurons each and SiLU activations. To train the model, we use Adam optimizer with a learning rate of  $10^{-3}$  and a weight decay of  $10^{-4}$ . We use an exponential learning rate scheduler with a decay rate of 0.99. To integrate the vector-fields, we use `dopri5` provided in `torchdiffeq` [52] with `atol = rtol =  $10^{-5}$` . All experiments are performed using a single NVIDIA H100 GPU.

### C.1 Artificial Benchmark 1: 1-dimensional problem with input function dependent correlation

We have considered two sets of experiments, one where the training and inference resolution is the same ( $N_x = 128$ ), and another where the training resolution is coarser than the inference resolution (training on  $N_x = \{8, 16, 32, 64\}$  and inference on  $N_x = 128$ ). For both sets of experiments, the configurations are tabulated in table C1

Figure C1 illustrates samples of the generated high-fidelity function using FLORA and FLORAL along with the absolute error when trained with 1000 high-fidelity training samples. Here, the low-fidelity and high-fidelity training and inference resolutions are all set to 128 discretization points. Figure C2 compares the RMSE, NRMSE, and CRMSE metrics of the proposed multi-fidelity probabilistic neural operator framework against single-fidelity baselines. As shown in fig. C3, even when the model is trained at a reduced resolution of 64 discretization points and evaluated at 128 points ( $2\times$  resolution increase), the predictive uncertainty is still reduced.

### C.2 1-dimensional advection equation

For training the models, the configurations are tabulated in table C2. Figure C4 illustrates the absolute error in the solution obtained using the low-fidelity model, FLORA, and FLORAL on unseen initial conditions when trained with 5000 high-fidelity training samples. We use the same initial conditions as in fig. 8, and, as shown, increasing the number of high-fidelity training samples improves predictive accuracy and reduces predictive uncertainty for both models.

Table C2: Training configurations for the 1-dimensional advection equation. The training and inference resolutions are common across spatial and temporal resolutions. The number of Fourier modes is common to both spatial and temporal dimensions.

<b>Train→Infer Resolution</b>	<b>Epochs</b>	<b>Train Size</b>	<b>Validation Size</b>	<b>Batch Size</b>	<b># Fourier Modes</b>
128 → 128	500	500	1,000	16	64
		1,000		64	
		5,000		128	

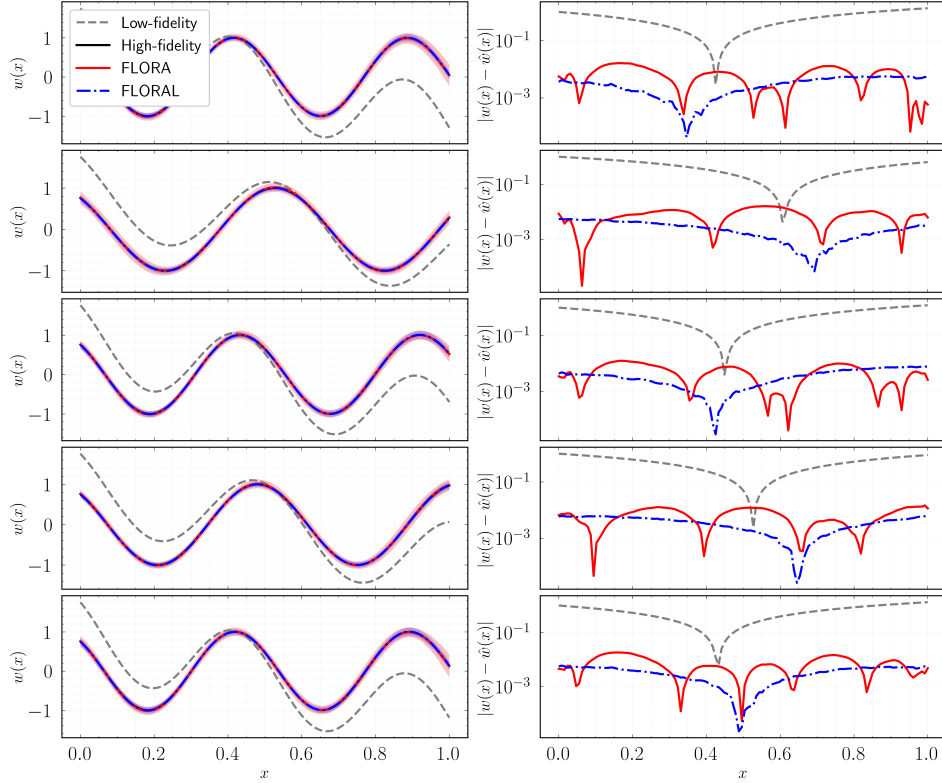


Figure C1: Samples of the generated high-fidelity function (left) using FLORA (—) and FLORAL (---) and the absolute error (right) for the 1-dimensional problem with input function correlation. The shaded region indicates  $\pm 10$  standard deviations about the mean for both models, computed using 100 generated ensembles. Model trained with 10 high-fidelity and corresponding low-fidelity training samples for a training and inference resolution of 128 discretization points. Samples are generated on the same input function as in fig. 3.

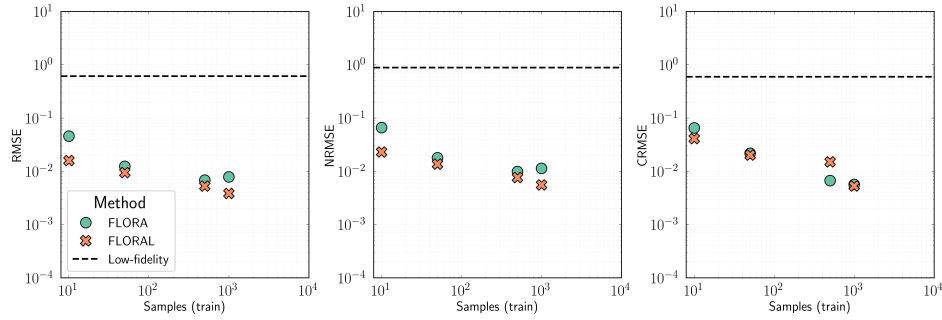


Figure C2: Comparison of RMSE (left), NRMSE (center), and CRMSE (right) for the 1-dimensional problem with input function dependent correlation. To compute the statistics, 1000 unseen high-fidelity function samples are used, and for each sample, 100 ensembles are generated for the probabilistic models. Training and inference resolution set to 128 discretization points.

### C.3 1-dimensional burgers equation

For training the models, the configurations are tabulated in table C3. Figure C5 illustrates the absolute error in the solution obtained using the low-fidelity model, FLORA, and FLORAL on unseen initial conditions when trained with 5000 high-fidelity training samples. We use the same initial conditions as in fig. 11, and, as shown, increasing the number of high-fidelity training samples improves predictive accuracy and reduces predictive uncertainty for both models.

### C.4 Darcy flow

For training the models, the configurations are tabulated in table C4. Figure C6 illustrates the absolute error in the solution obtained using the low-fidelity model, FLORA, and FLORAL on unseen

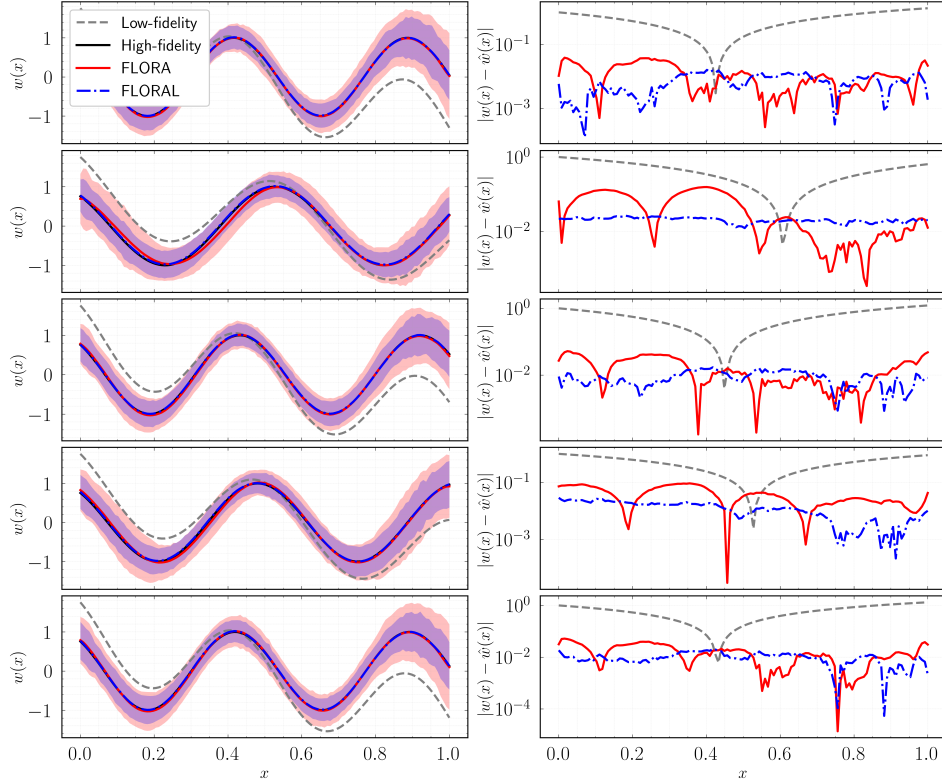


Figure C3: Samples of the generated high-fidelity function (left) using FLORA (—) and FLORAL (---) and the absolute error (right) for the 1-dimensional problem with input function correlation. The shaded region indicates  $\pm 10$  standard deviations about the mean for both models, computed using 100 generated ensembles. Model trained with 10 high-fidelity training samples using 64 discretization points, and inference is performed on 128 points, that is, a  $2\times$  resolution increase. Samples are generated on the same input function as in fig. 3.

Table C3: Training configurations for the 1-dimensional Burgers' equation. The training and inference resolutions are common across spatial and temporal resolutions. The number of Fourier modes is common to both spatial and temporal dimensions.

Train→Infer Resolution	Epochs	Train Size	Validation Size	Batch Size	# Fourier Modes
128 → 128	500	500	1,000	16	64
		1,000		64	
		5,000		128	

permeability fields when trained with 5000 high-fidelity training samples. We use the same permeability fields as in fig. 14, and, as shown, increasing the number of high-fidelity training samples improves predictive accuracy and reduces predictive uncertainty for both models.

Table C4: Training configurations for the Darcy flow. The training and inference resolutions are common across spatial and temporal resolutions. The number of Fourier modes is common to both spatial and temporal dimensions.

Train→Infer Resolution	Epochs	Train Size	Validation Size	Batch Size	# Fourier Modes
128 → 128	500	500	1,000	16	64
		1,000		64	
		5,000		128	

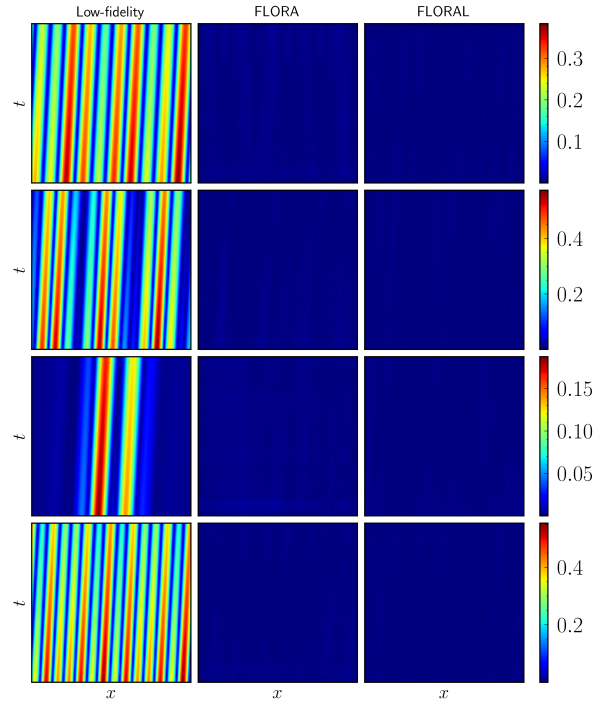


Figure C4: Illustration of absolute error in the solution obtained using low-fidelity model (left), FLORA (center), and FLORAL (right) on unseen initial conditions for the 1-dimensional advection equation. Model trained with 5000 high-fidelity and corresponding low-fidelity training samples. To compute the mean prediction for probabilistic models, 50 ensembles are generated for each unseen initial condition. Samples are generated on the same initial conditions as in fig. 8.

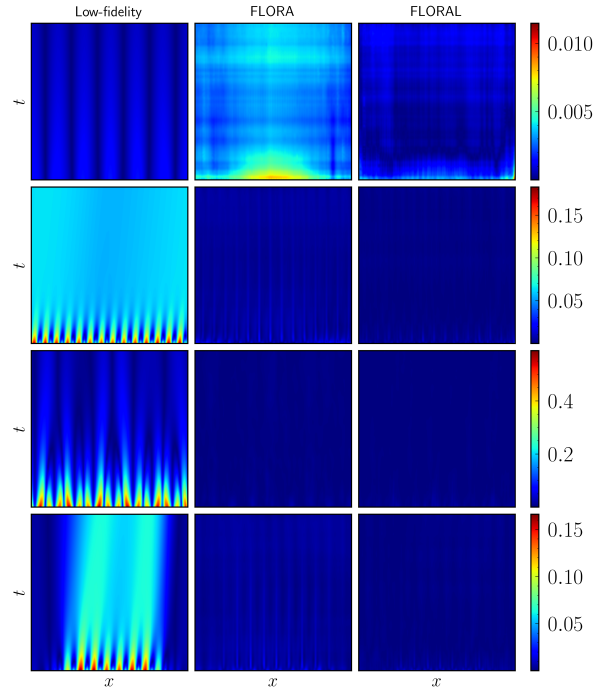


Figure C5: Illustration of absolute error in the solution obtained using low-fidelity model (left), FLORA (center), and FLORAL (right) on unseen initial conditions for the 1-dimensional Burgers' equation. Model trained with 5000 high-fidelity training samples and corresponding low-fidelity training samples. To compute the mean prediction for probabilistic models, 50 ensembles are generated for each unseen initial condition. Samples are generated on the same initial conditions as in fig. 11.

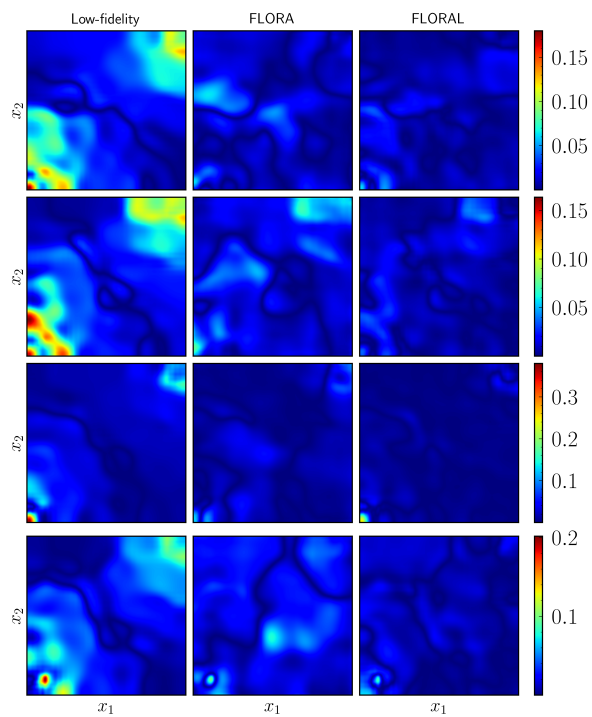


Figure C6: Illustration of absolute error in the solution obtained using low-fidelity model (left), FLORA (center), and FLORAL (right) on unseen permeability fields for the Darcy flow. Model trained with 5000 high-fidelity training samples and corresponding low-fidelity training samples. To compute the mean prediction for probabilistic models, 50 ensembles are generated for each permeability field. Samples are generated on the same permeability fields conditions as in fig. 14.